This is the preprint version of the following article: Kong, Y., & Guan, M. (2023). Hydro-mechanical simulations aid demand-oriented design of slit dams for controlling debris flows, debris avalanches and rock avalanches. Engineering Geology, 326, 107314 which is available at https://doi.org/.10.1016/j.enggeo.2023.107314.

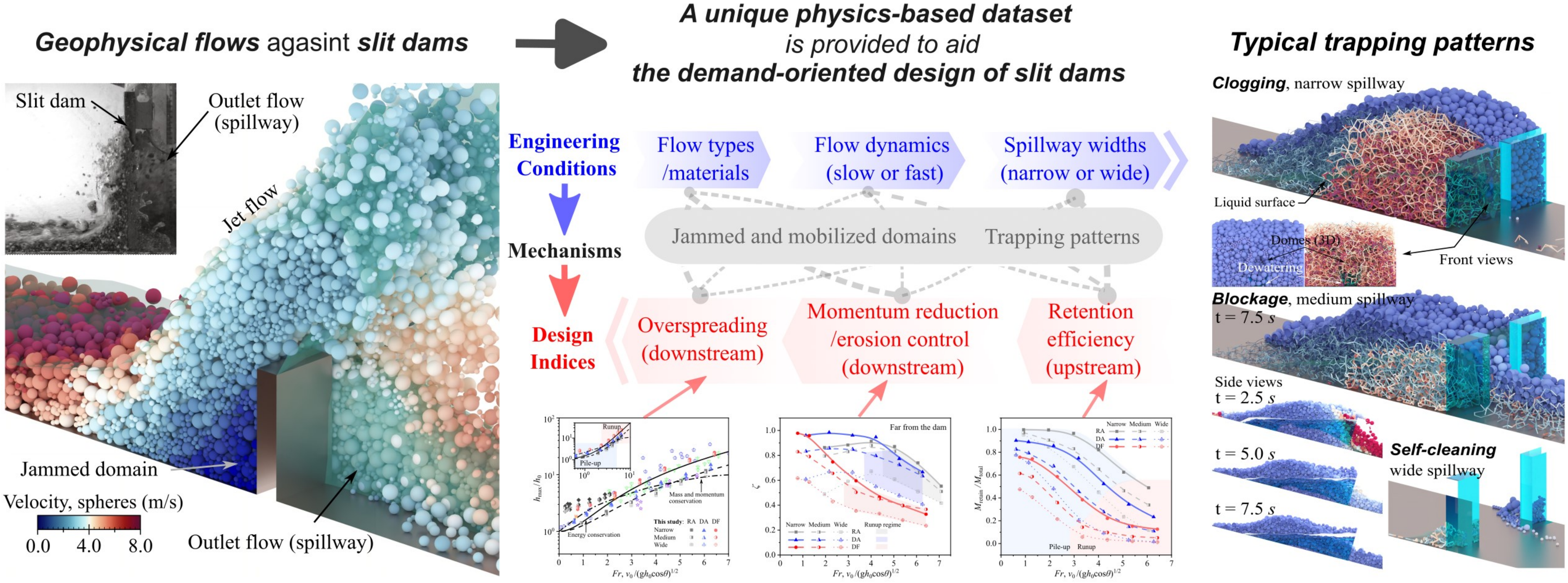

Dr. Yong Kong, affiliated with the Hong Kong Polytechnic University at the time of final publication.

Hydro-mechanical Simulations Aid Demand-oriented Design of Slit Dams for Controlling Debris Flows, Debris Avalanches and Rock Avalanches

Yong Kong[1], and Mingfu Guan[1†]

[1]Department of Civil Engineering, The University of Hong Kong, Hong Kong SAR, China.

[†]Corresponding author: Mingfu Guan (mfguan@hku.hk)

Abstract:

Slit dams have served as a reliable and effective countermeasure to mitigate geophysical flows, which can cause severe social, economic and environmental impacts. However, designing these dams to meet specific demands has been challenging due to the difficulties in quantifying the intricate interplay among flow properties, dam configurations and design objectives. This study utilizes explicit hydro-mechanical simulations to systematically evaluate critical design indices of slit dams in arresting debris flows, debris avalanches, and rock avalanches. The high-fidelity simulations reasonably capture essential physics observed in experiments, such as clogging, blockage, and self-cleaning traps. Furthermore, unified design diagrams are compiled from multiple perspectives to quantitatively link flow properties (fluid contents and *Fr* conditions) and spillway width to crucial design indices, including overspilling dynamics, downstream momentum reduction ratio ζ, and retention efficiency. The results reveal that: *i*) *Fr* exhibits nonlinear correlations with these design indices that vary significantly during the impact regime transitions from pile-up to runup, due to the resulting changes in the size and shape jammed and mobilized domains; *ii*) Both ζ and retention efficiency negatively correlate with fluid content, *Fr*, and spillway width, with different priorities; and *iii*) Fluid contents and *Fr* jointly govern overspilling dynamics, while increasing spillway width effectively reduces retention efficiency by changing trap patterns. In summary, this study contributes valuable insights into flow-dam interactions and offers a unique physics-based dataset to facilitate the demand-oriented design of slit dams for mitigating various anticipated flows.

Keywords: geohazard mitigation, debris flow, avalanche, slit dam, hydro-mechanical modeling, CFD-DEM

1. Introduction

Geophysical flows, such as avalanches, debris flows and floods, are dangerous natural hazards (Agliardi et al., 2020; Iverson et al., 2011; Li et al., 2022; Yin et al., 2023) that are expected to become more frequent and severe due to climate and landcover changes (Ayat et al., 2022; Bozzolan et al., 2023; Kaitna et al., 2023; Zhang et al., 2023). Slit dams are widely used as an effective countermeasure to mitigate the impacts of these hazards for diverse objectives, including community and infrastructure protection (Hungr et al., 1984; Lucas-Borja et al., 2021), erosion and torrent control (Baggio and D'Agostino, 2022; Marchi et al., 2019), moderate water and sediment flows (Campisano et al., 2014; Lucas-Borja et al., 2019), retaining large boulders and woods (Piton et al., 2022; Wang et al., 2022), and agricultural land development (Abbasi et al., 2019; Piton et al., 2017). However, the current design of slit dams relies mainly on engineering experience and simplified models (e.g., Lucas-Borja et al., 2021; Piton et al., 2022; Piton and Recking, 2016), which limits their effectiveness. The status quo has been largely limited by the difficulties in capturing and quantifying the interplay between realistic flow properties, various dam configurations, and case-specific design requirements. Consequently, a comprehensive quantitative analysis of this interplay using a physics-based dataset remains elusive, particularly for multiphase flows.

Slit dams typically have one or several spillways (i.e., slits or culverts) that allow fluid and finer grain-size sediment to pass through while trapping boulders and woods (Piton et al., 2020). A narrow spillway (Figure 1a) can quickly become jammed or clogged if excessive debris enters at once, while a wider spillway (Figure 1d) produces a slower build-up and smaller size of jammed domains. In addition, the impinging flow properties (i.e., wet versus dry, slow versus fast, Figures 1b, 1c, 1e, and 1f) can also strongly affect mechanical jamming. Current research on this phenomenon has primarily focused on dry granular flows (e.g., Choi et al., 2020; Marchelli et al., 2020; Wu et al., 2022) and theoretical analysis (Piton et al., 2022). However, a fundamental question remains regarding the mechanics of jammed and mobilized domains formed in geophysical flows of various natures (e.g., wet versus dry) against slit dams with different spillways. Furthermore, the effects of these domains on overspilling, energy-breaking, and trapping behavior remain poorly understood, partly because of the lack of reliable data obtained under realistic and controlled conditions.

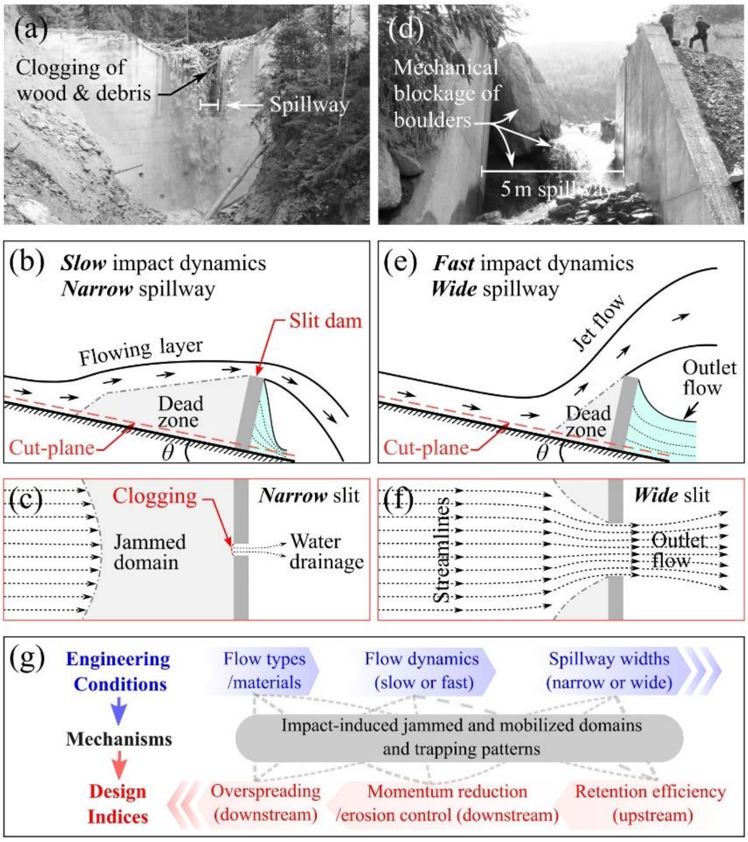

Figure 1. Field photos (a) and (d) show slit dams arresting geophysical flows with relatively narrow and wide spillways, respectively (Photos modified: *a* from Mühlburger, 2015 and *b* from Piton and Recking, 2016). Sketches (side view *b* and cut-plane view *c*) of a slow impinging flow against a slit dam with a narrow spillway. Illustrations (side view *e* and cut-plane view *f*) of a fast impinging flow against a slit dam with a wide spillway. (g) An overview of the interplay between engineering conditions (flow materials, flow dynamics, and spillway widths) and design indices for the design of slit dams.

Existing studies on geophysical flows against slit dams are described by four methodological categories: field, experimental, theoretical, and numerical approaches. Field investigations have reported in-depth analyses of the environmental effects of slit dams (Chiu et al., 2021; Huang et al., 2021; Lucas-Borja et al., 2021). However, these studies are mainly presented as case studies conducted in particular environments (Lucas-Borja et al., 2021), and thus their main findings often remain confined to the local contexts. Furthermore, existing experimental studies are dominated by laboratory-scale flume tests (Choi et al., 2016, 2020; Wu et al., 2022; Zhou et al., 2019), which provided valuable data and helped to offer a better understanding of the key controlling factors of impact behavior. However, they are limited mainly by idealized flow materials, various constraints, minimal pre-impact Froude number ranges, and difficult-to-estimated quantities. Moreover, many physical studies focused on the impact load or hydraulic conditions while lacking quantitative indices for evaluating the overspilling dynamics, trapping and energy-breaking efficiencies (Armanini and Larcher, 2001; Hu et al., 2020; Rossi and Armanini, 2019). The abovementioned complexity also surpasses the applicability of hydraulic formulas (Armanini and Larcher, 2001) or theoretical predictions (Piton et al., 2022).

Alternatively, many numerical methods have been utilized to investigate geophysical flows against slit structures, including discrete-based methods (Discrete Element Method (DEM), Goodwin and Choi, 2020; Marchelli et al., 2020; Zhou et al., 2020), continuum-based methods (Computational Fluid Dynamics (CFD), Aydin et al., 2022; Bernard et al., 2019; Material Point Method (MPM), Li et al., 2020; Smoothed Particle Hydrodynamics (SPH), Yang et al., 2021), and coupled approaches (SPH-DEM, Canelas et al., 2017; CFD-DEM, Kong et al., 2022a). However, the majority of studies on slit dams have focused on dry granular flows using DEM, which is utterly out of proportion to its practical importance. As slit dams are typically constructed to arrest geophysical flows with fluid, theories and findings based on dry granular flows are of limited use to engineers. In addition, Piton et al. (2022) reported that explicit hydro-mechanical models of boulder-laden flows are too computationally demanding to study boulder jamming associated with slit dams. Nevertheless, the authors' recent study (Kong et al., 2022a) successfully applied the unified CFD-DEM method to perform large-scale hydro-mechanical simulations on debris flows against flexible, slit and rigid barriers, with a primary focus on analyzing debris-flow impact loads acting on different barriers.

To facilitate the demand-oriented design of slit dams, this study endeavors to establish quantitative relationships between engineering conditions and critical design indices (Figure 1g) via the following efforts:

(i) Obtaining a unique physics-based dataset by performing systematic hydro-mechanical simulations on debris flows and debris/rock avalanches against slit dams with narrow, medium, and wide spillways (Figure 2);

(ii) Elucidating the reasons behind different overspilling, energy-breaking, and trapping behavior by revealing how engineering conditions alter the impact-induced jammed and mobilized domains (Figures 3 and A1) and typical trapping patterns (Figure 7);

(iii) Compiling unified design diagrams to quantitatively link flow properties (fluid contents and Froude conditions) and spillway width to crucial design indices, including overspilling (Figure 4), momentum reduction (Figure 6), and retention efficiency (Figure 8).

2. Methods and model setup

A unified CFD-DEM coupled method is utilized to probe the dynamics of debris flows and debris/rock avalanches against slit dams. For example, a debris flow is treated as a mixture of a continuous slurry and discrete gap-graded particles (Figure 2b), using CFD and DEM, respectively. The two-way coupling between CFD and DEM modules describes the fluid-solid interactions in a debris flow. The fluid is controlled by the locally-averaged Navier-Stokes equation for each fluid cell, while the motions of a particle are governed by Newton's equations. This method has been widely adopted to investigate granular-fluid systems relevant to geomechanics (Li et al., 2021; Kong et al., 2023) and industry (Goniva et al., 2012; Yu and Zhao, 2022). The code used to capture the complicated fluid-solid interactions has been developed and validated in previous works (e.g., Li et al., 2021; Zhao and Shan, 2013), particularly the multiphase flow-barrier interactions (Kong et al., 2021b, 2022a, 2022b). For convenience, this work provides a brief overview of the key ingredients of the employed method for modeling geophysical flows, slit dams, and their interactions.

2.1. Basic formulations for modeling multiphase geophysical flows

The coarse solid materials in geophysical mass flows (e.g., debris flows/avalanches and rock avalanches) are modeled by DEM. The translational and rotational motions of a solid particle i are governed by the following Newton's equations:

$$m_i \frac{d\boldsymbol{U}_i^{\mathrm{p}}}{dt} = \sum_{j=1}^{n_i^{\mathrm{c}}} \boldsymbol{F}_{ij}^{\mathrm{c}} + \boldsymbol{F}_i^{\mathrm{f}} + \boldsymbol{F}_i^{\mathrm{g}} \tag{1}$$

$$I_i \frac{d\boldsymbol{\omega}_i}{dt} = \sum_{j=1}^{n_i^{\mathrm{c}}} (\boldsymbol{M}_{\mathrm{t},ij} + \boldsymbol{M}_{\mathrm{r},ij}) \tag{2}$$

where m_i and I_i denote the mass and momentum of inertia of particle i, respectively. $\boldsymbol{U}_i^{\mathrm{p}}$ and $\boldsymbol{\omega}_i$ are the translational and angular velocities of particle i, respectively. n_i^{c} is the total number of contacts for particle i. $\boldsymbol{F}_{ij}^{\mathrm{c}}$, $\boldsymbol{M}_{\mathrm{t},ij}$ and $\boldsymbol{M}_{\mathrm{r},ij}$ represent the contact force, tangential torque, and rolling torque imposed on particle i from particle j or the walls, respectively. $\boldsymbol{F}_i^{\mathrm{g}}$ is the gravitational force of particle i. $\boldsymbol{F}_i^{\mathrm{f}}$ is the fluid-solid interaction force acting on the particle i. In particular, four fluid-solid interaction forces, namely drag, buoyancy, viscous, and virtual mass forces, are considered. Moreover, this work uses spherical particles with rolling resistance, which accounts for particle shape and roughness and thus improves the simulations of a geophysical flow and its interactions with slit dams (Otsubo et al., 2017).

In a free surface geophysical mass flow, the fluid system, i.e., air and viscous liquid (composed of water and fine-solid materials), is modeled by discretized fluid cells with the finite-volume method in CFD. The following continuity equation and locally averaged Navier-Stokes equation are solved by the Finite Volume Method (FVM) for each fluid cell:

$$\frac{\partial(\varepsilon_{\mathrm{f}}\rho_{\mathrm{f}})}{\partial t}+\nabla\cdot(\varepsilon_{\mathrm{f}}\rho_{\mathrm{f}}\boldsymbol{U}^{f})=0 \tag{3}$$

$$\frac{\partial(\varepsilon_{\mathrm{f}}\rho_{\mathrm{f}}\boldsymbol{U}^{\mathrm{f}})}{\partial t}+\nabla\cdot\left(\varepsilon_{\mathrm{f}}\rho_{\mathrm{f}}\boldsymbol{U}^{\mathrm{f}}\boldsymbol{U}^{\mathrm{f}}\right)=-\nabla p-\boldsymbol{f}^{\mathrm{p}}+\varepsilon_{f}\nabla\cdot\boldsymbol{\tau}+\varepsilon_{\mathrm{f}}\rho_{\mathrm{f}}\mathbf{g}+\boldsymbol{f}^{\mathrm{s}} \tag{4}$$

where $\boldsymbol{U}^{\mathrm{f}}$ and p represent the averaged velocity and pressure for the fluid phase in a cell, respectively. $\boldsymbol{g}$ is the gravitational acceleration. ε_{f} is the void fraction. $\boldsymbol{f}^{\mathrm{p}}$ is the interaction force acting on the fluid in a cell imposed by particle(s) inside the cell. $\boldsymbol{f}^{\mathrm{s}}$ denote the surface tension force. The liquid-air interface is determined algebraically from phase fractions, and the phase fraction distribution is smeared over a few fluid cells with the Volume-of-Fluid (VOF) method (von Boetticher et al., 2016).

The three-dimensional expressions of stress tensor $\boldsymbol{\tau}$ in Eq. (4) for Newtonian and non-Newtonian fluids can be simplified to constitutive functions. In this work, the air is modeled as a Newtonian fluid, represented by:

$$\tau=\mu_{\mathrm{f}}\dot{\gamma} \tag{5}$$

where τ, μ_f and $\dot{\gamma}$ denote the shear stress, viscosity, and shear rate of the fluid, respectively. On the other hand, the liquid phase in a debris flow is simulated as a non-Newtonian fluid using the widely-applied Herschel-Bulkley equation (Coussot et al., 1998):

$$\tau=\tau_0+\kappa\dot{\gamma}^n \tag{6}$$

where τ_0 and κ denote the yield stress and consistency index of the fluid, respectively. The exponent n represents the flow index, where $n < 1$ represents shear thinning fluid, $n > 1$ corresponds to a shear-thickening fluid, and $n = 1$ leads to a Bingham fluid. Slurry and mudflow typically have a flow index smaller than 1 (Kostynick et al., 2022).

Details of the fluid-solid interactions, the three-phase VOF method, the two-way coupling procedures, as well as particle-particle and particle-wall contacts can be found in Supporting Information S1.

2.2. Model setup and test program

Figure 2a illustrates the geometric model setup for a geophysical flow against a slit dam constructed on a low-gradient inclined channel with a slope angle θ = 15°. The CFD domain is bounded by four no-slip channel walls, an upper atmosphere face, and an outlet face at the end of the channel (Figure 2a). Only fluid cells in a mixture sample are initially filled with viscous slurry, while the rest of the CFD domain is filled with air (Figures 2c and 2d). In DEM, the bottom and both sides of the flow channel are modeled as frictional rigid walls. Slit dams are modeled as no-slip boundary walls in CFD and frictional rigid walls in DEM. In this study, the spillway width b is varied, and it is commonly quantified by a dimensionless size factor, i.e., the transverse blockage b/w (Marchelli et al., 2020), where w = 1.8 m is the channel width. The ratios for slit dams with narrow, medium and wide spillways (Figures 2c, 2d and 2e) are 0.11, 0.33 and 0.56, respectively. b/w = 1 corresponds to an undisturbed chute flow under No Barrier (NB) conditions, which can be used as comparison tests to determine the downstream momentum reductions (see Sect. 3.3). Conversely, b/w = 0 represents a closed-type check dam that extends the entire width of the channel (Kong et al., 2021a).

Figure 2b depicts a typical debris flow modeled as a mixture of a viscous slurry and gap-graded tridisperse particles. Each material governs the flow behavior differently (Iverson (1997); Pudasaini and Mergili, 2019). Regarding interstitial fluid, the viscous slurry in a debris flow is treated as a Herschel-Bulkley fluid (Remaître et al., 2005). Although a fixed rheological formula cannot accurately predict natural debris flow (Iverson, 2003), the Herschel-Bulkley model with shear thinning rheology best describes the interstitial fluid in a debris-flow mixture (Coussot et al., 1998; Kostynick et al., 2022). In the solid phase, 22,125 tridisperse particles are generated in each case with a maximum particle size ratio of 3. The relative post spacing, represented by the spillway width to the maximum particle diameter ratio ($b/d_{\max}$), is a crucial parameter that directly influences the trapping or regulation function of a slit dam, as highlighted in previous studies (Zhou et al., 2019; Gong et al., 2021). We consider typical values of $b/d_{\max}$ for dams with narrow, medium, and wide spillways as 1.67, 5, and 8.33, respectively. Key parameters adopted in simulations are summarized in Table 1.

The inset in Figure 2b shows a laboratory flume test by Rossi and Armanini (2019), where a fast-flowing mixture of water and sediments with Froude number > 3 impacted a slit structure. Froude number (Fr) is a widely used parameter for characterizing flow dynamics and designing various countermeasures (Rossi and Armanini, 2019; Kong et al., 2022a), calculated as $Fr = v_0/\sqrt{gh_0 cos\theta}$, where v_0 and h_0 denote pre-impact flow velocity and depth. They observed abundant flow characteristics, including *i*) the formation of a vertical jet, *ii*) the jet propagating upward, becoming wider and decelerating, and *iii*) the flow partially trapped upstream of the dam, while part of the material passed through the spillway. In comparison,

Figure 2b displays the simulated impact dynamics of a debris flow (Fr = 4.3) against a slit dam, demonstrating reasonable consistency with the experimental observations in the inset. The observed difference between the experiment and simulation is mainly related to the barrier-flow height ratio, which can significantly affect the impact behavior (Faug et al., 2015; Kong et al., 2023). Furthermore, distinct differences in flow redirection, deceleration, and separation, as well as overtopping and passing through slit dams, can be observed among representative debris flow (DF), debris avalanche (DA), and rock avalanche (RA) cases (Figures 2c, 2d and 2e) in Figures 3 and A1 in the following sections, as well as supplementary movies S1 and S2 (https://doi.org/10.25442/hku.22208008.v1; Kong and Guan, 2023).

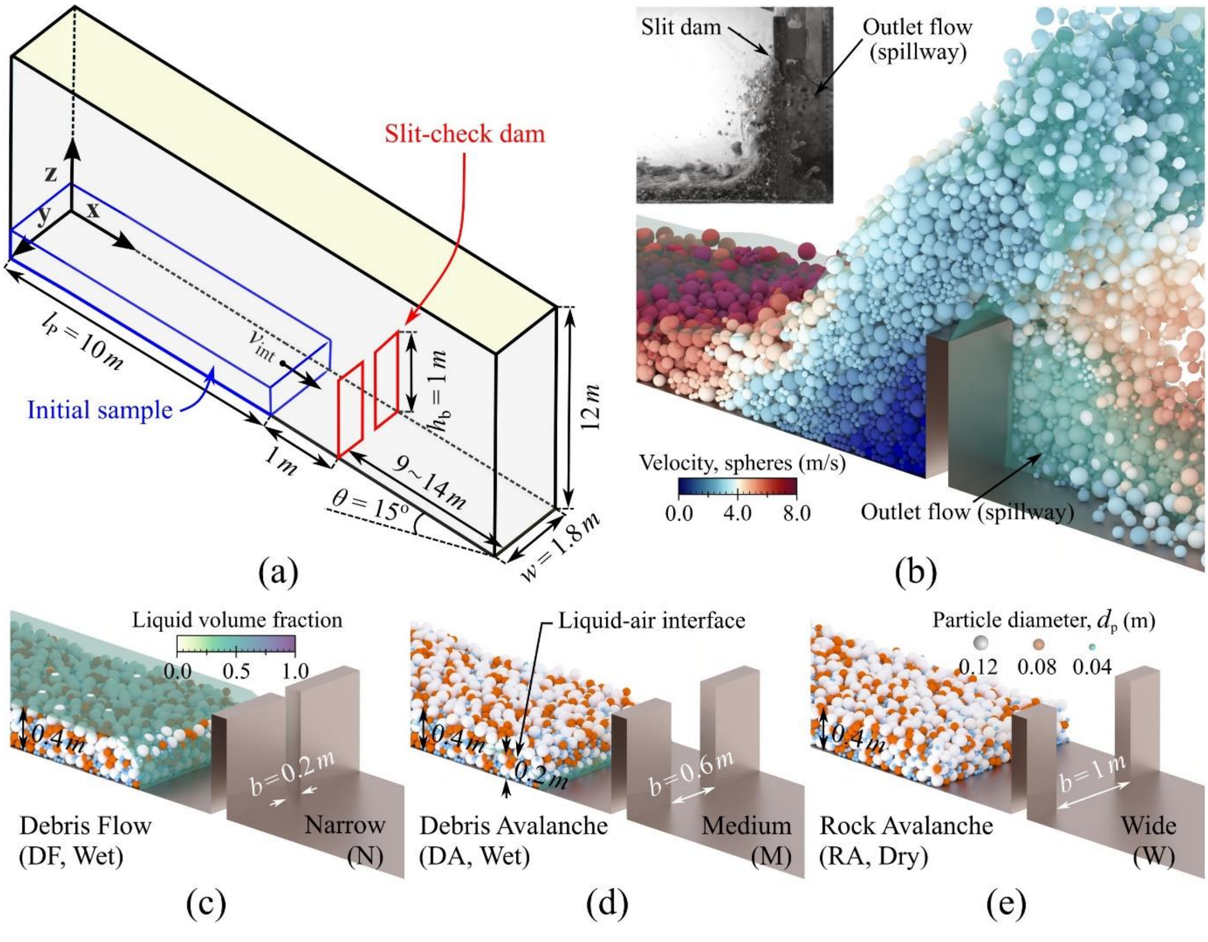

Figure 2. Model setup. (a) Model geometry prior to the release of the initial sample with an initial velocity v_{int}. (b) presents the simulated impact dynamics of a debris flow with v_{int} = 8 m/s against a slit dam. The inset in (b) is a side picture from the laboratory flume test by Rossi and Armanini (2019). (c), (d) and (e) show oblique views of debris flow (fully saturated), debris avalanche (partially saturated) and rock avalanche (dry) impacting slit dams with narrow, medium, and wide spillways, respectively.

Table 1. Key parameters used in simulations

Items	Properties	Values
Particle [a]	Particle number	22125

	Density * [kg/m^3]	2500
	Radius [m]	0.02, 0.04, and 0.06
	Young's modulus (particle-particle contact) [GPa]	70
	Young's modulus (particle-wall contact) [GPa]	700
	Poisson's ratio *	0.3
	Restitution coefficient *	0.7
	Interparticle friction coefficient	0.7
	Particle-wall friction coefficient	0.7
	rolling friction coefficient *	0.1
Air [a]	Density [kg/m^3]	1
	Viscosity [Pa·s]	1.48×10^{-5}
Slurry [b]	Density [kg/m^3]	1350
	Consistency index [Pa·s^n]	21.30
	Flow index	0.24
	Yield stress [Pa]	17.86
Simulation control	Cell size (CFD) [m]	0.2*0.2*0.2
	Time step (DEM) [s]	5×10^{-7}
	Time step (CFD) [s]	5×10^{-5}
	Simulated real time [s]	2 ~ 15

Notes: [a] Refer to the typical values of physical properties for geophysical flows (Iverson, 1997; Li et al., 2021); [b] Refer to typical values of the non-Newtonian fluids (Remaître et al., 2005).

To comprehensively investigate the effects of flow properties and dam configurations on the crucial design indices of slit dams, we conducted systematic DF, DA, and RA tests under varying pre-impact *Fr* numbers against slit dams with narrow (N), medium (M), and wide (W) spillways. The initial heights of the viscous slurries in DF, DA, and RA cases (Figures 2c, 2d and 2f) are set to 0.4 m, 0.2 m, and 0 m, respectively, making them fully saturated, partially saturated, and dry granular flows, respectively. Moreover, the samples, including the fluid and solid phases, are assigned with prescribed velocities (i.e., v_{int} = 1 ~ 14 m/s) before being released to flow down under gravity and impact a slit dam. As a result, a broad range of *Fr* numbers (i.e., *Fr* = 0.6 ~ 7.1) is produced for impinging flows with a pre-impact flow depth of h_0 ≈ 0.4 m. Furthermore, the bulk volume of the sample (~ 7.2 m^3) is chosen to ensure reasonable overflow duration in each simulation. For convenience, the test IDs are defined according to flow types (i.e., DF, DA, and RA), dam types (i.e., N, M, W, and NB), and v_{int}. For example, Case DF-W-V8 refers to the numerical test of a debris flow with v_{int} = 8 m/s impacting a slit dam with a wide-sized spillway.

Table 2 summarizes the test scenarios for the 84 cases. The computational time on an 8-core Intel CPU (3.7 GHz) desktop computer varied from 30 to 195 hours for each case, depending primarily on the simulated real-time (1.5 ~ 11.5 s) and flow materials (wet or dry).

Therefore, this study conducted large-scale (10^0 ~ 10^1 m) simulations instead of full-scale (10^1 ~ 10^2 m) simulations for computational efficiency. Furthermore, the adoption of particle sizes is determined according to the scale of the setup (Figure 2a). The number of particles along the flow width direction needs to be small enough to save computational cost and sufficiently large to avoid boundary effects from the lateral walls. In addition to flow dynamics, solid volume concentrations, and dam configurations, the flow-dam interactions can also be affected by the complexity of natural geophysical mass flows. For example, large boulders (Piton et al., 2022), broad particle size distributions (Cabrera and Estrada, 2021), phase separation of the solid and fluid components (Pudasaini and Fischer, 2020), varying flow depths (Iverson et al., 2016; Kong et al., 2023), and erosion (Pudasaini and Krautblatter, 2021) are common in nature and may affect the results presented below. These factors can be explored in future studies.

Table 2. Test program

Test groups	Initial velocity, v_{int} [m/s]				Pre-impact *Fr*
	Narrow (N)	Medium (M)	Wide (W)	No Barrier (NB)	
Debris Flow (DF)	1 ~ 12	1 ~ 12	1 ~ 12	1 ~ 12	0.8 ~ 6.4
Debris Avalanche (DA)	1 ~ 12	1 ~ 12	1 ~ 12	1 ~ 12	0.6 ~ 6.2
Rock Avalanche (RA)	2 ~ 14	2 ~ 14	2 ~ 14	2 ~ 14	0.9 ~ 7.1

3. Results and discussion

3.1. Impact-induced jammed and mobilized domains

Figure 3 compares critical profiles of the jammed and mobilized domains formed in twelve representative debris flow (DF) and rock avalanche (RA) cases, subjected to slow and fast impact dynamics against slit dams with varying spillways. The oblique, side and top cut-plane views in Figure 3a reveal distinct flow features and contact networks in key impact-induced physical processes, such as flow redirection, deceleration and separation, as well as overtopping and passing through a slit dam. Figure 3a displays velocity and contact fields in the oblique and side views, respectively, while the two right sub-figures show the top cut-plane pictures at $z = 0.5h_b$ of the two left views. Moreover, the comparison between the upper and lower panels highlight the differences in jammed and mobilized domains formed in wet and dry flows against a slit dam with the same v_{int}.

The upper panel in Figure 3b demonstrates the coexistence of jammed and mobilized domains in a debris flow case. The jammed domains, also known as dead zones (Faug, 2015; Kong et al., 2021a), are delimited by white dash-dotted lines and can be identified using a velocity threshold (i.e., below 5% of v_0; Faug et al., 2009). For mobilized domains, the side view displays the flowing layer upon jammed domains, while the top cut-plane pictures show the outlet flow between the two triangular jammed domains. In contrast, the mobilized domains include the flowing layer above the jammed domains (side view) and the outlet flow between the two jammed domains (top cut-plane pictures).

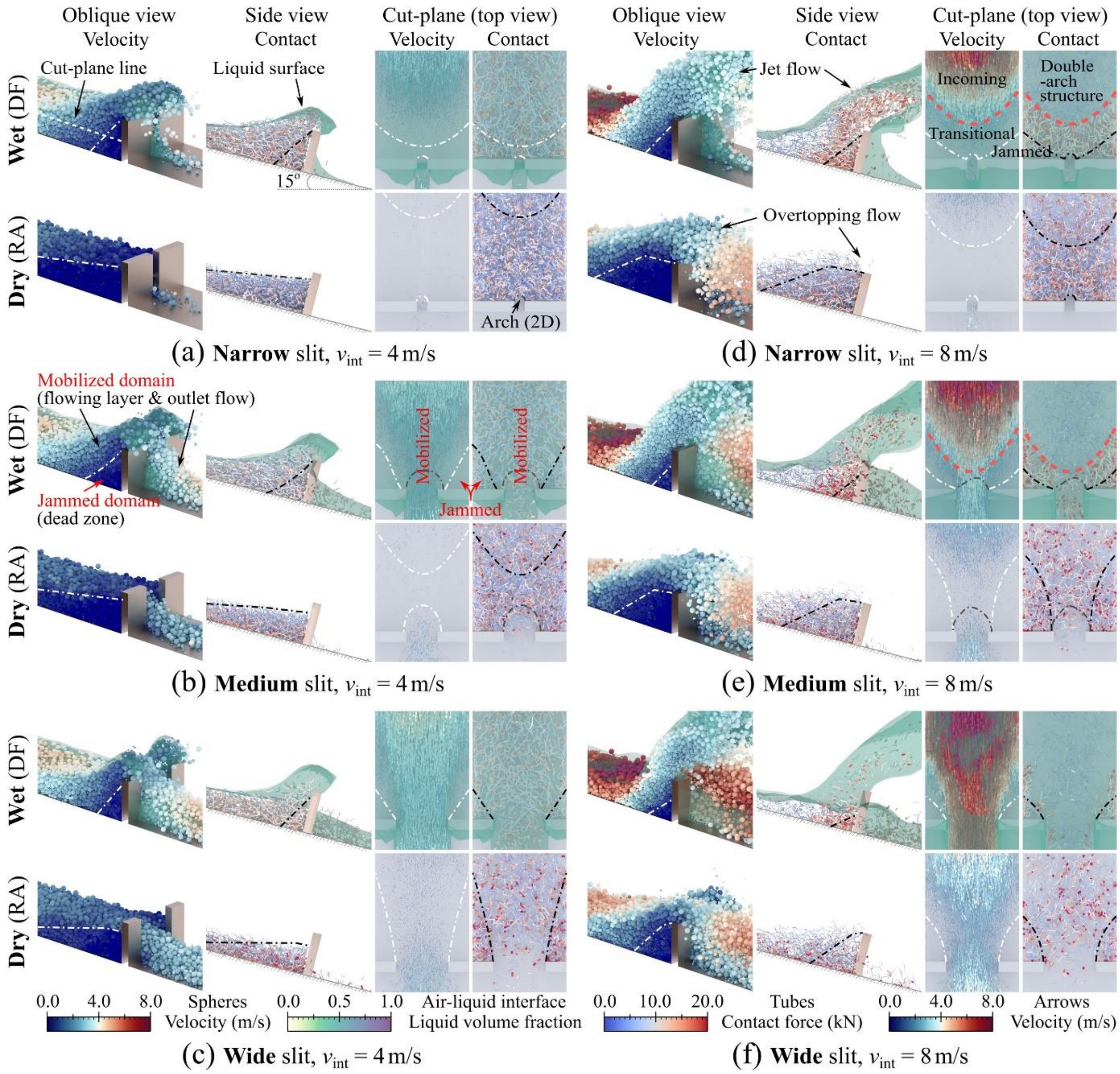

Figure 3. Comparison of the jammed and mobilized domains formed in representative wet (DF) and dry (RA) cases with v_{int} = 4 m/s (left panel) and 8 m/s (right panel) impacting slit dams with narrow (*a* and *d*), medium (*b* and *e*), and wide (*c* and *f*) spillways at *t* = 1 s.

Figure 3 reveals that flow materials, dynamics, and spillway widths influence the morphology and size of jammed domains with varying degrees of significance. Specifically, impinging flows with higher fluid content and faster impact dynamics generally result in smaller triangle-shaped jammed domains, whereas flows with lower fluid content and slower impact dynamics tend to produce larger trapezoid-shaped ones under Froude similarities (Li et al., 2021). This is likely attributed to the fact that flows with lower fluid contents tend to form more stable contact networks during the mobilized-jammed transition, resulting in a higher efficiency of energy dissipation than flows with higher fluid contents. Fundamentally, the fluid phase promotes flow mobility by reducing interparticle collisions and friction (Kaitna et al., 2016; Iverson, 2003), while grain shear stress is more effective in dissipating energy than fluid viscous shearing (Fang et al., 2021; Kong et al., 2022b). Moreover, flow properties dictate the flowing layer, while spillway width plays a crucial role in shaping the outlet flows. Flowing layers are similar for flows with the same materials and dynamics, regardless of the spillway width. Nonetheless, 2D arch structures only occur in cases with narrow and medium spillways (Figures 3a, 3b, 3d and 3e), whereas the wide spillway cases (Figures 3c and 3f) do not exhibit any mechanical blocking of outlet flows by arch structures.

Figures 3d-upper and 3e-upper show that fast-moving (v_{int} = 8 m/s) wet flows can cause double-arch structures of contacts under the jet impact mode (Rossi and Armanini, 2019), behind a slit dam with narrow and medium spillways. This contact field phenomenon reveals a transition from weak to strong contacts during the shift from free incoming flows to a deviation of the flowing layer upon jammed domains. To the best of the authors' knowledge, this phenomenon has not been observed in previous studies. In contrast, for dry flows with similar pre-impact *Fr* numbers as the two wet cases (Figures 3d and 3e), outside-inside jammed domains are formed by strong and more homogeneous interparticle contacts. This may be due to the lack of frequent contacts in highly mobilized domains for fast-moving wet free flows, where the fluid phase can dampen particle collisions and decrease interparticle friction. Conversely, in dry flows, dense contacts occur in both mobilized and jammed domains, indicating effective energy dissipation.

The impact-induced jammed and mobilized domains can evolve in a complex way and partially govern the overspilling dynamics (Sect. 3.2), downstream momentum reductions (Sect. 3.3), as well as trapping patterns and retention efficiency (Sect. 3.4) of the flow-dam interactions. In addition, interested readers can find the jammed and mobilized domains in six representative debris avalanche (DA) cases at t = 1 s in Figure A1 in Appendix A, with larger snapshots providing more details. Notably, the double-arch structures could also be observed in fast-moving (v_{int} = 8 m/s) DA cases with narrow and medium spillways.

3.2. Flow properties governing overspilling dynamics

The occurrence of overspilling flows induced by a slit dam in arresting geophysical flows poses a threat to downstream communities and infrastructure. Therefore, it is crucial to quantify the maximum overspilling height to design slit dams in areas where infrastructure or communities are located close to the dam. Figure 4 presents a unified design diagram that examines the impacts of Fr conditions, relative post spacing b/d_{max}, and flow types (DF, DA and RA) on the normalized maximum overspilling heights h_{max}/h_0, where h_{max} represents the maximum overspilling height. It is worth noting that the symbols used to represent our numerical results are consistent in Figures 4, 6c, 6d, and 8. To enable a comprehensive analysis, a unique dataset comprising normalized data from experiments (Armanini et al., 2020; Choi et al., 2016, 2020; Song et al., 2021a; Wu et al., 2022), analytical models (Li et al., 2021; Song et al., 2021b), and numerical results (Zhou et al., 2020) is plotted in Figures 4a and 4b for comparison.

Figure 4a displays positive correlations between h_{max}/h_0 and Fr, with the correlation trends primarily governed by flow types (DF, DA, and RA). A decrease in fluid content results in a decrease in h_{max}/h_0 under Fr similarities, which is consistent with experimental data (Wu et al., 2022). Additionally, h_{max}/h_0 values obtained from flume tests using dry glass bead flows (Choi et al., 2016, 2020) tend to be larger than those for RA cases, while experimental data of h_{max}/h_0 for mixture flows against rigid barriers (Armanini et al., 2020; Song et al., 2021a) match well with that of DF cases with slit dams. This indicates that the spillway has a negligible effect on the Fr-h_{max}/h_0 relationships. To verify this, we use a boxplot to show the influence of b/d_{max} on h_{max}/h_0 in Figure 4b. It should be noted that the boxplot represents numerical results for v_{int} = 2 ~ 12 m/s to ensure a basis for comparison among DF, DA, and RA cases. The results indicate that b/d_{max} has only a minor impact on h_{max}/h_0, which is consistent with data from studies with slit dams (Choi et al. 2016; Zhou et al. 2020). However, h_{max}/h_0 varies significantly at a given b/d_{max} (narrow, medium, or wide) in response to impinging flow types and dynamics. Additionally, Figure 4b suggests that the median and mean h_{max}/h_0 are slightly larger for a given flow type with b/d_{max} = 1.67 (narrow) than for b/d_{max} = 8.33 (wide).

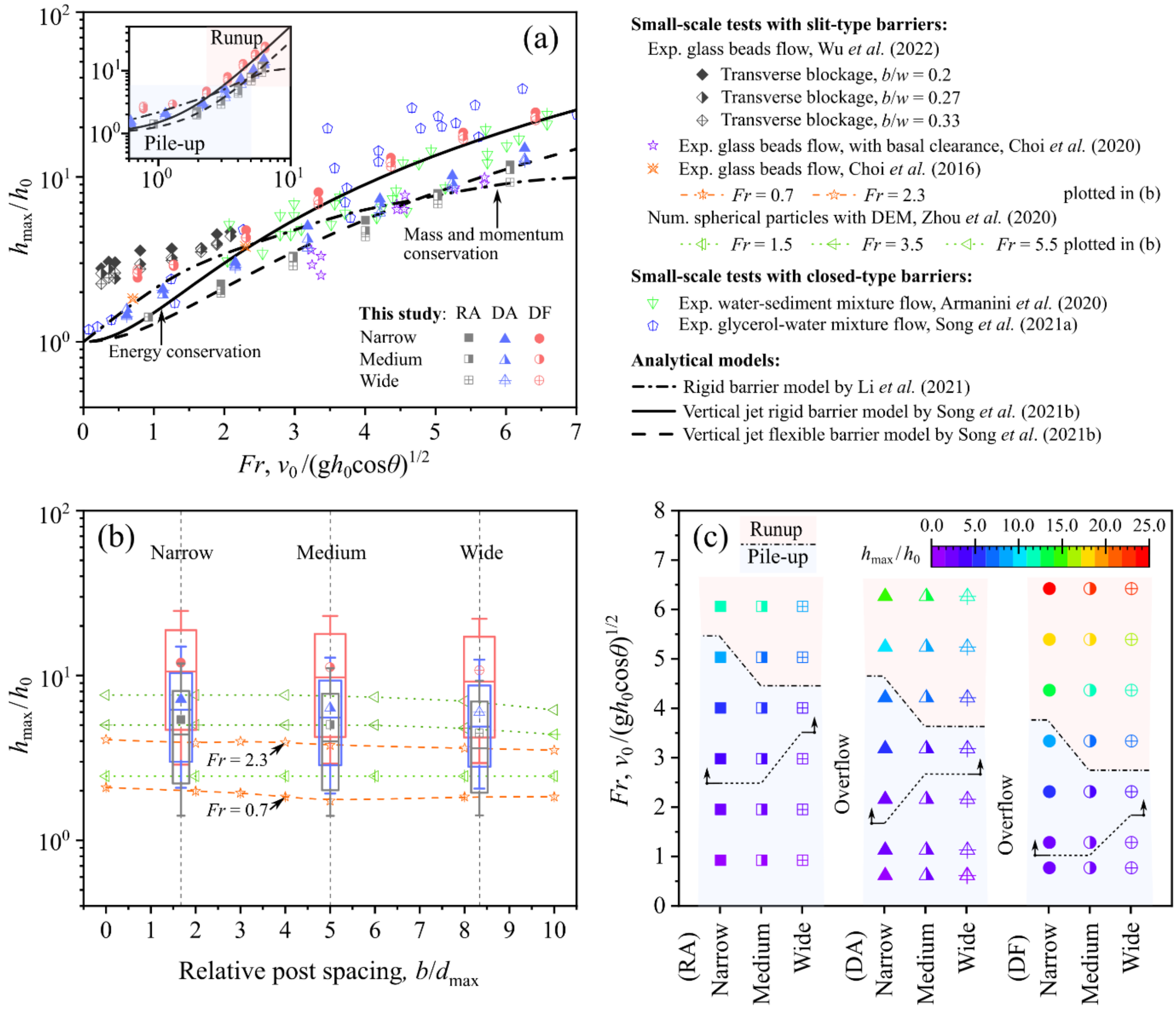

Figure 4. A unified design diagram quantifying the joint effects of flow properties (fluid contents and *Fr*) and relative post spacing $b/d_{\max}$ (narrow, medium and wide) on the normalized maximum overspilling height $h_{\max}/h_0$ for geophysical flows against slit dams. (a) presents $h_{\max}/h_0$ as a function of *Fr*. (b) displays $h_{\max}/h_0$ as a function of $b/d_{\max}$, using boxplots to depict the interquartile range, 5th and 95th percentiles, median, and mean. The width of boxes serves only to distinguish between flow types. A phase diagram (c) shows how pile-up to runup transition and overflow occurrence in each flow type affect the $h_{\max}/h_0$ (color of symbols). The shades of blue and orange denote regimes of pile-up and runup, respectively.

Moreover, the inset in Figure 4a, which features double-log plots, compares the numerical measures of Fr- h_{max}/h_0 relationships with popular analytical models. This comparison highlights the dominant impact regimes, namely pile-up and runup, which are crucial in selecting suitable design models for flow-resisting countermeasures (Kong et al., 2021a; Song et al., 2018; Ng et al., 2022a). This study identifies the primary impact regime by examining the shape of jammed domains when impinging flows first overspill a dam. The pile-up and runup regimes are primarily signaled by trapezoid- and triangle-shaped jammed domains (see side views in Figure 3), respectively. The inset in Figure 4a suggests that, for wet flows under pile-up regimes (slow impact dynamics), the analytical model based on mass and momentum conservation (Li et al., 2021) is superior in predicting h_{max}/h_0. Conversely, for DF cases under runup regimes (fast impact dynamics), the vertical jet rigid barrier model (Song et al., 2021b), derived from energy conservation, provides the best predictions of h_{max}/h_0. The vertical jet flexible barrier model (Song et al., 2021b) agrees with RA cases, possibly due to the ability of both types of barriers to enable partial materials to pass through.

Figure 4c provides further insight into the influence of flow types on h_{max}/h_0 (color of symbols), and how *Fr* and spillway width affect the pile-up to runup transition and overflow occurrence in each flow type. The results demonstrate that the pile-up to runup transition occurs at a lower *Fr* for wide spillways than narrow ones. This is primarily due to the smaller high-energy dissipative jammed domains formed with a wide spillway compared to a narrow one. Conversely, overflow occurs at a higher *Fr* for larger spillways because more debris passes through, resulting in less jammed debris serving as the pathway for overflow (see Figure 3).

In summary, this unified design diagram indicates that overspilling dynamics with a slit dam are primarily governed by flow types and *Fr* conditions, with spillway width having a minor impact. Therefore, engineers should select appropriate analytical models based on accurate predictions of anticipated flow fluid contents (flow types) and impact regimes (*Fr* conditions). To control overspilling, flow breakers or baffles can be installed upstream of the dam to reduce impact dynamics (Zhang and Huang, 2022; Rossi and Armanini, 2019), while deflectors on the dam can redirect overflow (Ng et al., 2017).

3.3. Near- and far-field downstream momentum reductions

Flow momentum is a critical factor influencing entrainment and impact characteristics of geophysical flows (Iverson et al., 2011; Pudasaini and Krautblatter, 2021). Slit dams have emerged as a practical solution to retard downstream flow rates and minimize the associated momentum flux. Figure 5 illustrates the time-series data of near- and far-field downstream momentum ϵ for representative wet and dry cases. Under the NB condition, the far-field Max(ϵ) is comparable to, or even greater than, the near-field Max(ϵ) for wet flows (Figures 5a and 5b). This phenomenon is primarily attributed to the ability of the fluid phase to diminish basal friction and instigate positive feedback, which raises flow speed and momentum. In contrast, such feedback becomes negative for undisturbed dry flows (Figures 5c and 5d).

The presence of a slit dam leads to a significant reduction in far-field Max(ϵ) as compared to undisturbed flows or near-field Max(ϵ) (Figure 5), primarily due to the flow-dam interactions and landing. The momentum loss from flow-dam interactions occurs because kinetic energy is converted to potential energy in overflows, and effective energy dissipation occurs due to frictional shearing and collisions among particles between mobilized and jammed domains. Furthermore, landing also leads to a significant loss of ϵ through complex mechanisms (e.g., hydraulic jump, oscillating jets, surface rollers, turbulence within the jump, and strong waves; Akan, 2021), which can be influenced by factors such as flow dynamics, landing angle, and flow materials (Ng et al., 2022b).

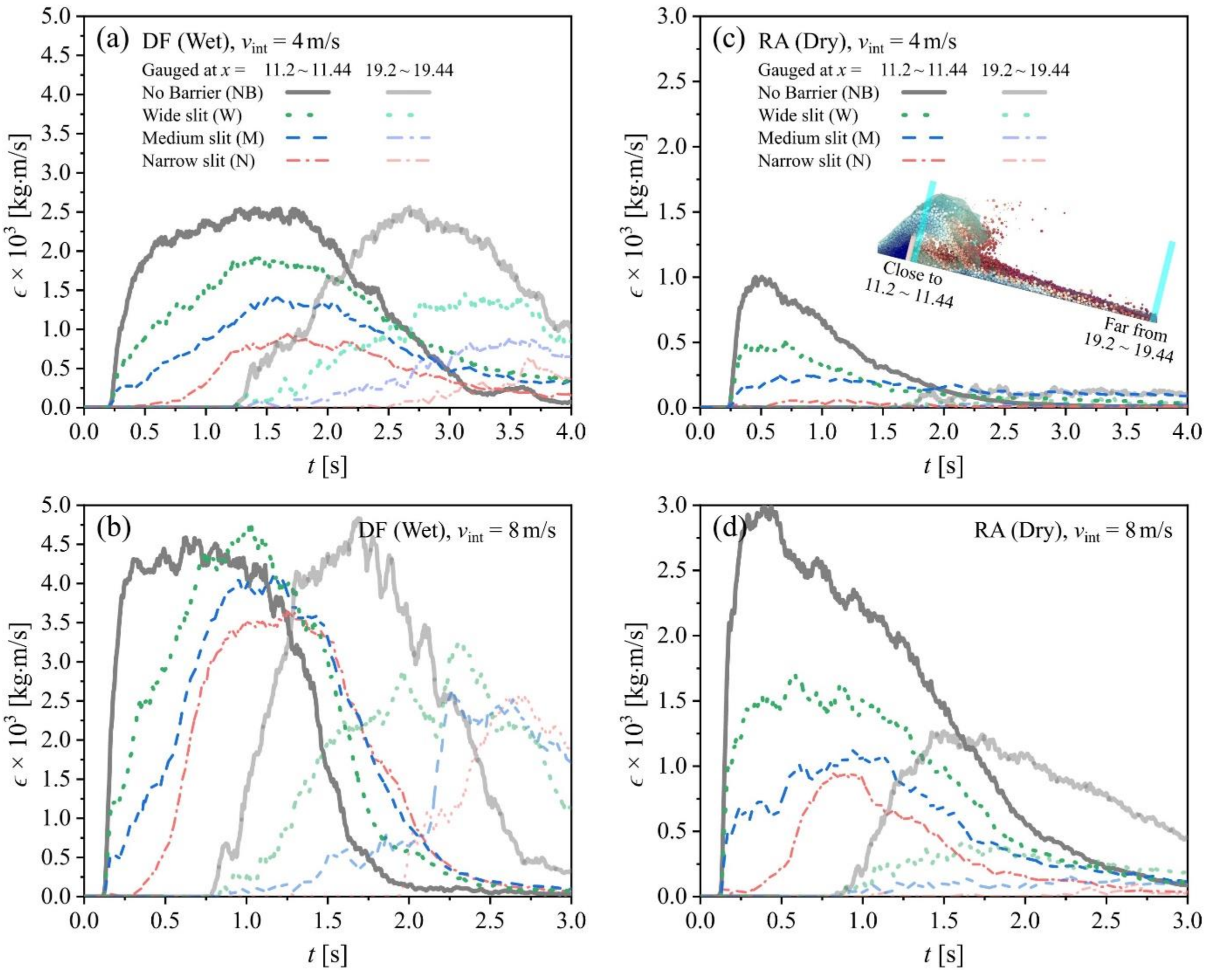

Figure 5. Time-series data of downstream momentum ϵ acquired at 11.2 m < x < 11.44 m (near-field) and 19.2 m < x < 19.44 m (far-field) in representative debris flows (a: v_{int} = 4 m/s and b: v_{int} = 8 m/s) and rock avalanches (c: v_{int} = 4 m/s and d: v_{int} = 8 m/s) impacting slit dams. The inset in Figure 5c provides a snapshot of Case DF-W-V8, highlighting the measured near- and far-field domains with a width of $2d_{\max}$.

Furthermore, the near-field Max(ϵ) typically decreases in the presence of a slit dam compared to free flows (Figures 5a, 5c and 5d). However, Figure 5b reveals that the near-field

Max(ϵ) in Case DF-W-V8 (v_{int} = 8 m/s, wide spillway) is slightly larger than that under the NB condition. This can be attributed to the formation of small jammed domains in the wide spillway case, causing a delay of a more significant peak discharge of overspill and outlet flows, resulting in a marginal increase in instantaneous ϵ. Despite this, the accumulative ϵ over time for Case DF-W-V8 remains smaller than that measured in free flows, indicating a loss of accumulative downstream momentum. Moreover, increasing spillway width contributes to the growth of Max(ϵ) because decreasing spillway width enables the formation of jammed domains at shorter timescales. This results in larger jammed domains, longer interfaces between mobilized and jammed domains, and more energy-dissipative frictional shearing and collisions. Note that time-series data of ϵ for representative DA cases (v_{int} = 4 m/s and 8 m/s) can be found in Figures A2a and A2b in Appendix A.

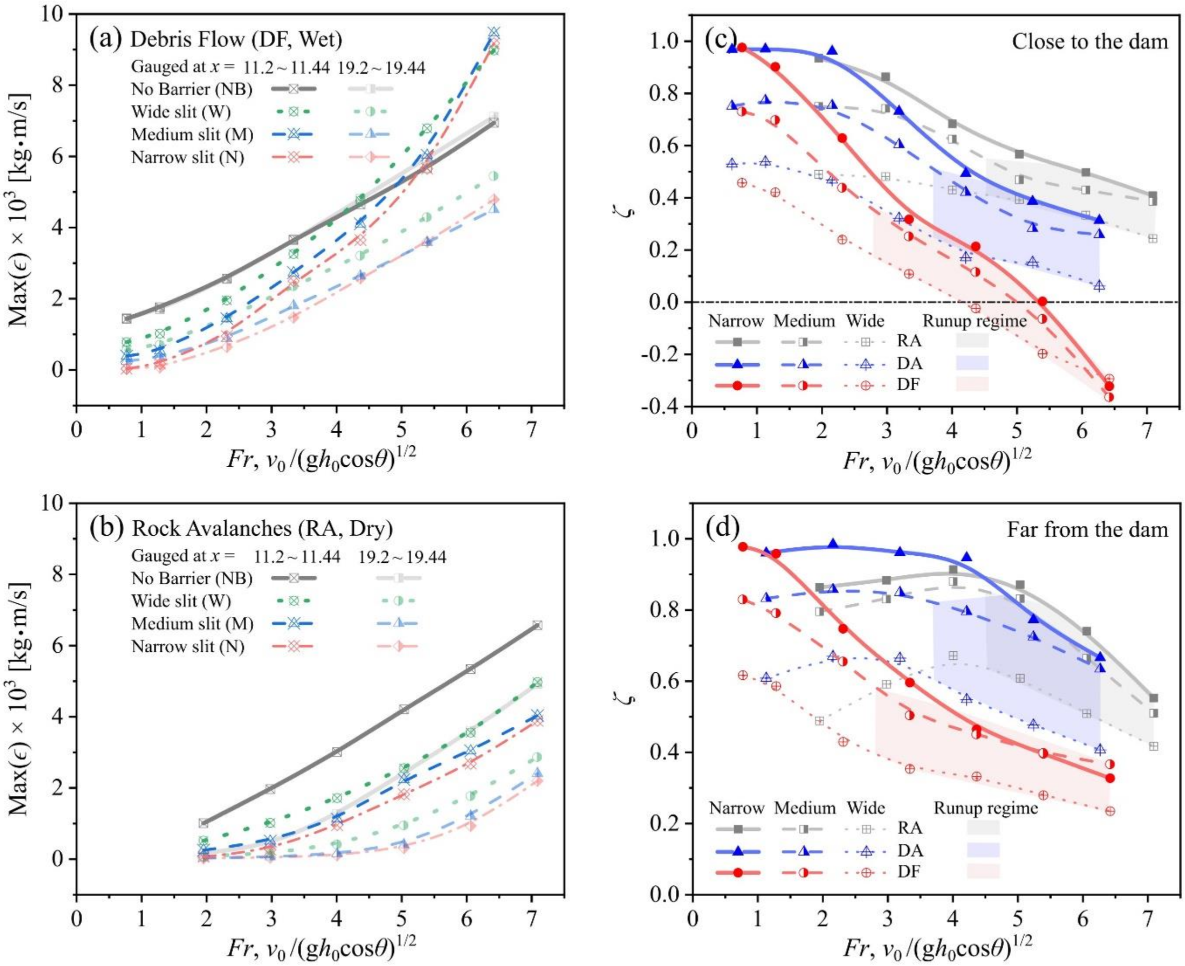

Figure 6. The near- and far-field maximum downstream momentums Max(ϵ) and their reduction ratios ζ as functions of *Fr* for geophysical flows impacting slit dams. (a) and (b) show the Max(ϵ) measured from wet (DF) and dry (RA) flows, respectively. (c) and (d) present the near- and far-field ζ obtained across all cases, respectively.

Figures 6a and 6b display the measured near- and far-field Max(ϵ) during the entire impact process for all DF and RA cases, respectively. Free flow cases (i.e., the NB condition) exhibit nearly linear positive correlations between Max(ϵ) and Fr, while the Max(ϵ) increases nonlinearly with rising Fr in the presence of a dam. This suggests that the effects of jammed domains on Max(ϵ) change with increasing Fr conditions. Furthermore, the Max(ϵ) generally decreases as the spillway width increases, except for DF cases with extremely high impact dynamics (i.e., v_{int} = 12 m/s). This exception is likely due to the greater momentum loss resulting from the interactions between mobilized (overflow and outlet flow) and jammed domains with a wide spillway, compared to that with a narrow spillway, under extremely high-speed impact dynamics. It is worth noting that the Max(ϵ) extracted from all DA cases is presented in Figure A2c in Appendix A.

Based on Figures 6a, 6b, and A2c, Figures 6c and 6d provide a comprehensive examination of the combined impact of flow types, dynamics, and spillway widths on the near- and far-field downstream momentum reduction ratio ζ, respectively. The ratio ζ is computed by subtracting the Max(ϵ) observed in the presence of a slit dam from the Max(ϵ) in free flows and dividing the result by the Max(ϵ) in free flows. Figure 6c highlights negative near-field Fr-ζ relations across all DF, DA, and RA cases, predominantly attributed to momentum loss caused by flow-dam interactions. Specifically, increasing Fr, spillway width, or water content creates smaller energy-dissipative jammed domains, resulting in a decline of the ratio ζ, albeit with varying priorities depending on impact regimes. For instance, as Fr increases, the effect of fluid content on the ratio ζ tends to increase. Intriguingly, the ratio ζ can take on negative values for DF cases when Fr exceeds 5, presumably because of the elevated peak flow discharge of overspill and outlet flows after a lag time. This finding is well-illustrated in Case DF-W-V8, as depicted in Figure 5b.

Figure 6d depicts the far-field Fr-ζ relations, which reflect the momentum loss caused by flow-dam interactions and landing. Unlike near-field Fr-ζ relations (Figure 6c), flow types (i.e., fluid content) primarily affect the trend of far-field Fr-ζ relations. Specifically, for DF cases, ζ continuously decreases with increasing Fr, while for DA and RA cases, ζ initially increases with Fr before exhibiting a continuous decrease, with inflection points located approximately after the occurrence of overflow and near the pile-up to runup transition (see Figure 3c). The observed trends arise from several critical processes, including the expansion of trapezoid-shaped jammed domains upstream under pile-up regimes, the reduction in jammed domain size after the pile-up to runup transition, and momentum loss at landing due to overflow.

Nonetheless, quantifying the relative contributions of these processes and the actual amount of momentum loss from each is currently impossible. The interplay between flow types, dynamics, and spillway widths drives these critical processes and the resulting far-field Fr-ζ relations.

3.4. Trapping patterns and retention efficiency

Slit dams are designed to intercept various materials in geophysical flows, such as sediment, boulders, and woods, thus reducing the density, velocity, and discharge rate of downstream flows (Huang et al., 2021; Piton et al. 2022). Figure 7 identifies three typical trapping patterns for debris avalanches against slit dams, including clogging with a narrow spillway (Figure 7a), blockage with a medium spillway (Figure 7b), and self-cleaning with a wide spillway (Figure 7c).

Figure 7a demonstrates that a clogging trap operates by exploiting the frictional properties of particles. The narrow spillway restricts the flow, leading to the jamming of large particles (Figure 7a-1-left), which form stable contact networks (Figure 7a-1-right) capable of withstanding loads. The frontal views depict the three-dimensional dome structure (Figures 7a-1), while the cut-plane pictures show the two-dimensional arch (Figures 7a-2). It is worth noting that the dome structure has rarely been revealed in previous numerical or experimental studies, especially for mixture flows against slit dams.

Figure 7b illustrates a blockage trap phenomenon, characterized by the absence of permanent arches in 2D and domes in 3D, observed behind a slit dam with a medium-sized spillway. Notably, weak and non-stable arches can form in medium-sized spillway cases (see Figures 3b, 3e, and A1-d). The debris continues to experience progressive shear collapse or fluid-sheared particle transport (Figures 7b-1 ~ 7b-3), even though jammed particles have obstructed the upstream channel during or after the main impact process (Figure 3b). It is noteworthy that for both clogging and blockage traps, the fluid still flows through the solid particles that are restrained by the slit dam (Figures 7a-1 and 7b-1 ~ 7b-3). Furthermore, Figure 7c shows a self-cleaning trap, where the majority of the material does not accumulate permanently behind the slit dam (Goodwin and Choi, 2020). The spillway is too broad to form any restraining structures upstream or within it, and hence no particles are retained in the spillway.

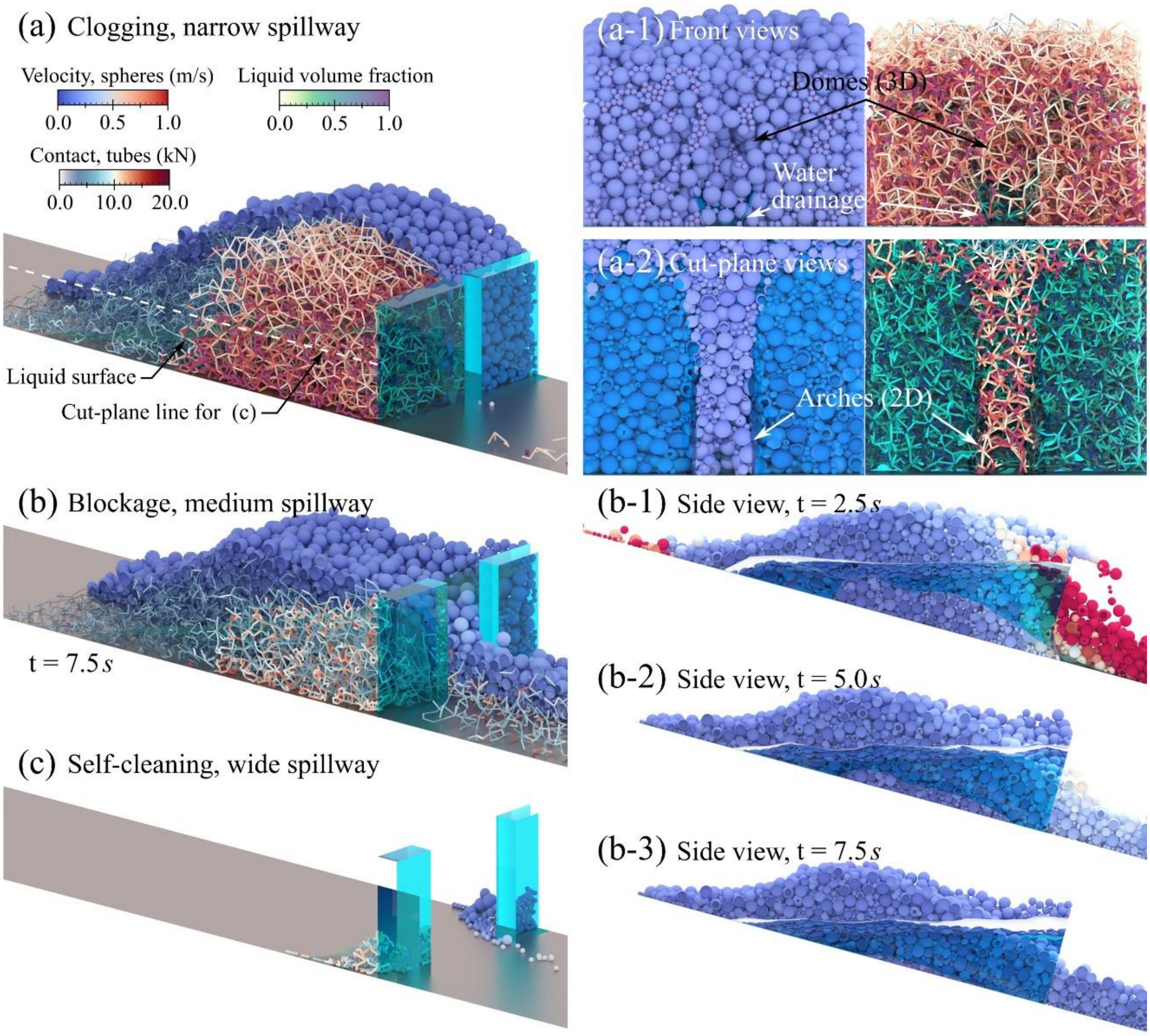

Figure 7. Snapshots show typical trapping patterns of slit dams in arresting debris avalanches: (a) clogging with a narrow spillway, (b) blockage with a medium spillway, and (c) self-cleaning with a wide spillway. The left-panel split views display liquid surface and interparticle contacts in the front half-space as well as gap-graded particles and debris fluid in the back half-space. (a-1) and (a-2) show the domes (frontal view) and arches (cut-plane view at $z = 0.5h_{\mathrm{b}}$) formed in a clogging trap, respectively. (b-1), (b-2), and (b-3) provide time sequence evidence of the progressive shear collapse in the flowing mass for the trapping pattern of blockage.

Figure 8 presents a unified design diagram that examines the joint influences of Fr, fluid contents, and relative post spacing b/d_{max} on the retention efficiency $M_{\mathrm{retain}}/M_{\mathrm{total}}$ and trapping patterns for slit dams in arresting geophysical flows. The ratio $M_{\mathrm{retain}}/M_{\mathrm{total}}$ is defined as the debris mass retained divided by a dam by the total initial debris mass (Gong et al., 2021). Additionally, a valuable dataset of $M_{\mathrm{retain}}/M_{\mathrm{total}}$ comprising previous experiments (Choi et al., 2016; Zhou et al., 2019) and simulations (Gong et al., 2021) is plotted in Figures 8b and 8c for comparison.

Figure 8a indicates that $M_{\mathrm{retain}}/M_{\mathrm{total}}$ is negatively correlated to Fr, fluid contents, and $b/d_{\max}$. These negative correlations are generally consistent with the results (Figures 8a and 8c) extracted from small-scale flume tests using granular-water mixture flows against slit dams (Zhou et al., 2019). However, Figure 8b shows that only minimal pre-impact Fr ranges were obtained for flows with the same fluid content (Zhou et al., 2019). Moreover, the experiments conducted by Choi et al. (2016) using glass bead flows produced Fr values lower than 2.5. Thus, Figure 8 presents a more comprehensive representation of the correlations, offering a complete understanding of the effects of Fr, fluid contents, and $b/d_{\max}$ on $M_{\mathrm{retain}}/M_{\mathrm{total}}$. Specifically, reducing Fr may not be effective in increasing $M_{\mathrm{retain}}/M_{\mathrm{total}}$ in DF cases with $Fr > 4$ or under runup regimes (Figure 8a), which has not been observed before.

Figure 8c highlights the adverse impact of $b/d_{\max}$ on $M_{\mathrm{retain}}/M_{\mathrm{total}}$. The boxplots of our numerical results offer statistical insights into the nonlinear Fr-$M_{\mathrm{retain}}/M_{\mathrm{total}}$ relations for different flow types. Specifically, for DF cases, the median (line) is lower than the average (circle symbols), and the lower whisker spans a narrower range compared to the upper whisker, in contrast to RA cases. These observed differences are primarily attributable to fluid contents, given the similar Fr ranges for different flow types presented in boxplots. Moreover, to reinforce our findings and enhance the understanding of the $b/d_{\max}$-$M_{\mathrm{retain}}/M_{\mathrm{total}}$ relations, Figure 8c also includes previously reported positive correlations between $M_{\mathrm{retain}}/M_{\mathrm{total}}$ and particle aspect ratio (Gong et al., 2021) and negative correlations between $M_{\mathrm{retain}}/M_{\mathrm{total}}$ and Fr (Choi et al., 2016) or water contents (Zhou et al., 2019).

Figure 8d presents a phase diagram that illustrates the interplay between $M_{\mathrm{retain}}/M_{\mathrm{total}}$ (symbol color), spillway widths, trapping patterns, and impact regime transitions. The diagram highlights the significant role of spillway width in determining trapping patterns. Specifically, the cases with narrow ($b/d_{\max}$ = 1.67) and medium ($b/d_{\max}$ = 5) spillways are identified as clogging and blockage traps, respectively. In contrast, cases with wide spillways ($b/d_{\max}$ = 8.33) are identified as self-cleaning traps only for highly fast-moving wet flows (green shades in Figure 8d), with the rest of the cases identified as blockage traps. Furthermore, Figure 8d shows that the transition from red to blue symbols (i.e., $M_{\mathrm{retain}}/M_{\mathrm{total}} \sim 0.5$ in this study) generally coincides with the pile-up to runup transition, irrespective of flow type and spillway width. This is primarily due to the sharp shifts in the shape and size of the impact-induced jammed domains during impact regime transitions.

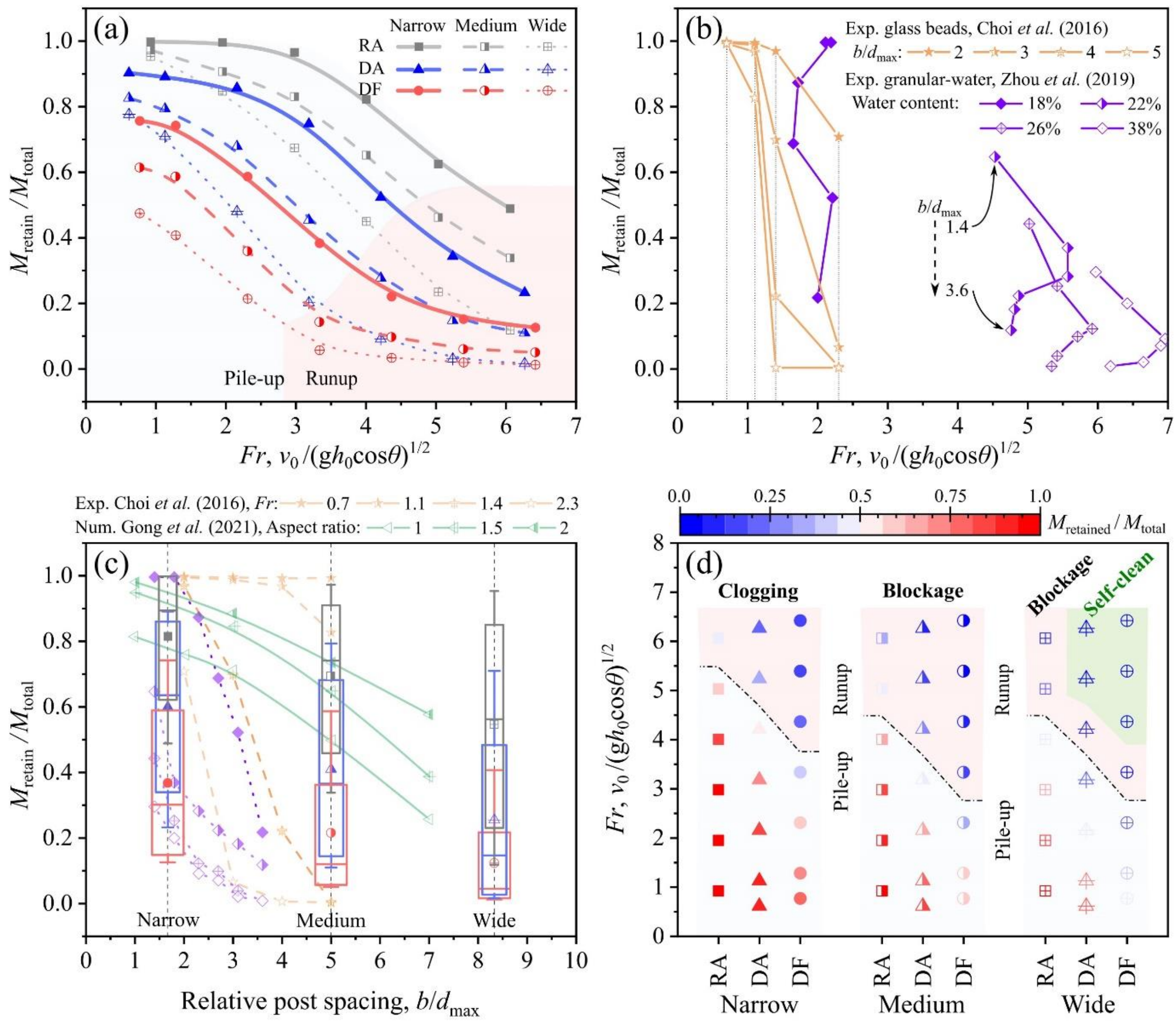

Figure 8. A unified design diagram quantifying the influences of flow properties (fluid contents and *Fr* conditions) and spillway widths on the retention efficiency $M_{\text{retain}}/M_{\text{total}}$ and trapping patterns of slit dams in arresting geophysical flows. (a) and (b) present $M_{\text{retain}}/M_{\text{total}}$ as a function of *Fr* obtained from this study and extracted from experiments, respectively. (c) shows $M_{\text{retain}}/M_{\text{total}}$ as a function of relative post spacing b/d_{max}, using boxplots to depict the interquartile range, 5th and 95th percentiles, median, and mean. The phase diagram (d) displays $M_{\text{retain}}/M_{\text{total}}$ (color of symbols) in conjunction with trapping patterns and impact regime transitions. The blue and orange shades denote pile-up and runup regimes, respectively.

4. Conclusions

This study presents systematic, hydro-mechanical simulations of geophysical flows of variable natures against slit dams, which has been rarely achieved in prior research. The employed CFD-DEM model captures essential physical phenomena observed in experiments. We focus on understanding and quantifying the interplay between flow properties (fluid contents and *Fr* conditions), spillway widths and critical design indices by scrutinizing impact-induced jammed and mobilized domains, overspilling, energy-breaking and trapping dynamics from multiple perspectives. The main results and findings are summarized as follows:

(a) Systematic high-fidelity simulations enable us to examine the impact-induced jammed and mobilized domains and to identify clogging, blockage and self-cleaning traps in a phase diagram. The results reveal that: (*i*) Flow properties (wet versus dry, slow versus fast) and spillway width jointly influence the shape and size of jammed domains, with different priorities; (*ii*) Impinging flows with higher fluid contents and faster impact dynamics tend to produce triangle-shaped, smaller jammed domains, while the opposite leads to trapezoid-shaped, larger domains; (*iii*) We observe, for the first time, double-arch contact structures in several fast-moving wet flow cases, displaying sharp transitions from weak to strong contacts during the shifts from free incoming flows to a deviation of the flowing layer upon jammed domains; and (*iv*) Spillway width primarily determines trapping patterns, whereby a clogging trap features with dome and arc structures, while a blockage trap typically forms weak and non-stable arches.

(b) We compile unified design diagrams that integrate multiple perspectives and combine physics-based numerical measures from this work and previously reported experimental, numerical, and analytical results. These diagrams quantitatively link flow properties (fluid contents and Fr conditions) and spillway width to crucial design indices, including the normalized maximum overspilling height h_{max}/h_0, downstream momentum reduction ratio ζ, and retention efficiency. We find that: (*i*) For overspilling, increasing spillway width has a minimal effect on reducing h_{max}/h_0, whereas decreasing fluid content or Fr can effectively reduce h_{max}/h_0; (*ii*) Both ζ and retention efficiency negatively correlate with fluid content, Fr, and spillway width, with different priorities; (*iii*) Increasing spillway width can significantly reduce retention efficiency by altering trapping patterns, while decreasing Fr is not effective in improving retention efficiency for debris flow cases under runup regimes; and (*iv*) Fr exhibits highly nonlinear correlations with h_{max}/h_0, ζ, and retention efficiency, whose trends are primarily determined by fluid content and vary significantly during the impact regime transitions from pile-up to runup, mainly due to the resulting changes in the shape and size of jammed domains.

This study and its findings offer a unique physics-based dataset that bridges the gap between engineering conditions and design indices, providing valuable insights for the demand-oriented design of effective flow-resisting slit dams based on anticipated geophysical flow properties.

CRediT authorship contribution statement

Yong Kong: Conceptualization, Methodology, Software, Visualization, Investigation, Validation, Writing – original draft. **Mingfu Guan**: Supervision, Funding, Data curation, Investigation, Writing – review & editing.

Data availability statement

The supplementary videos (Figures 2 and 3) and dataset (Figures 4, 5, 6, 8, and A2) underlying this article are permanently archived at https://doi.org/10.25442/hku.22208008.v1 (Kong and Guan, 2023).

Declaration of competing interest

The authors declare no competing interests.

Acknowledgments

This work was supported by the University Grants Council of Hong Kong (RGC/GRF Project #17202020) and the Guangdong-Hong Kong-Macau Technology Research Programme (Type C Project #SGDX20210823103537035).

Appendix A. Flow structure and downstream momentum for debris avalanches

Figure A1 is a supplementary figure for Figure 3 presented in Sect. 3.1 and compares the impact-induced jammed and mobilized domains that form during debris avalanches with v_{int} = 4 m/s and 8 m/s impacting different slit dams at t = 1 s. As supplementary figures for Figures 5 and 6 presented in Sect. 3.3, Figure A2 presents time-series data of the downstream momentum ϵ and the Max(ϵ) in debris avalanches against slit dams with narrow, medium and wide spillways. Figures A2a and A2b also include the ϵ and Max(ϵ) extracted from free flows (i.e., no barrier condition) for comparison.

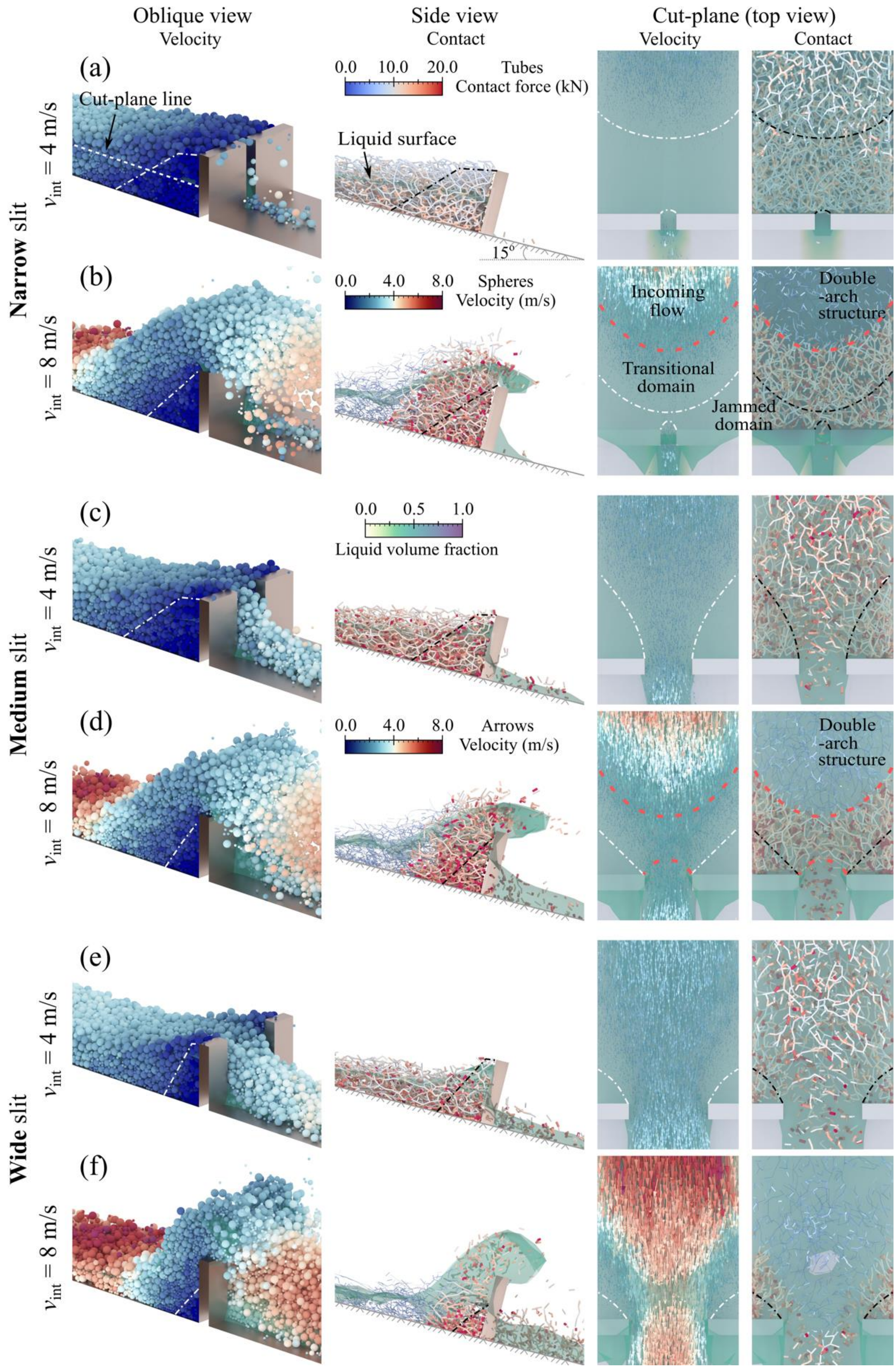

Figure A1. Comparison of the jammed and mobilized domains of debris avalanches with v_{int} = 4 m/s and 8 m/s impacting slit dams with narrow (*a* and *b*), medium (*c* and *d*), and wide (*e* and *f*) spillways at t = 1 s.

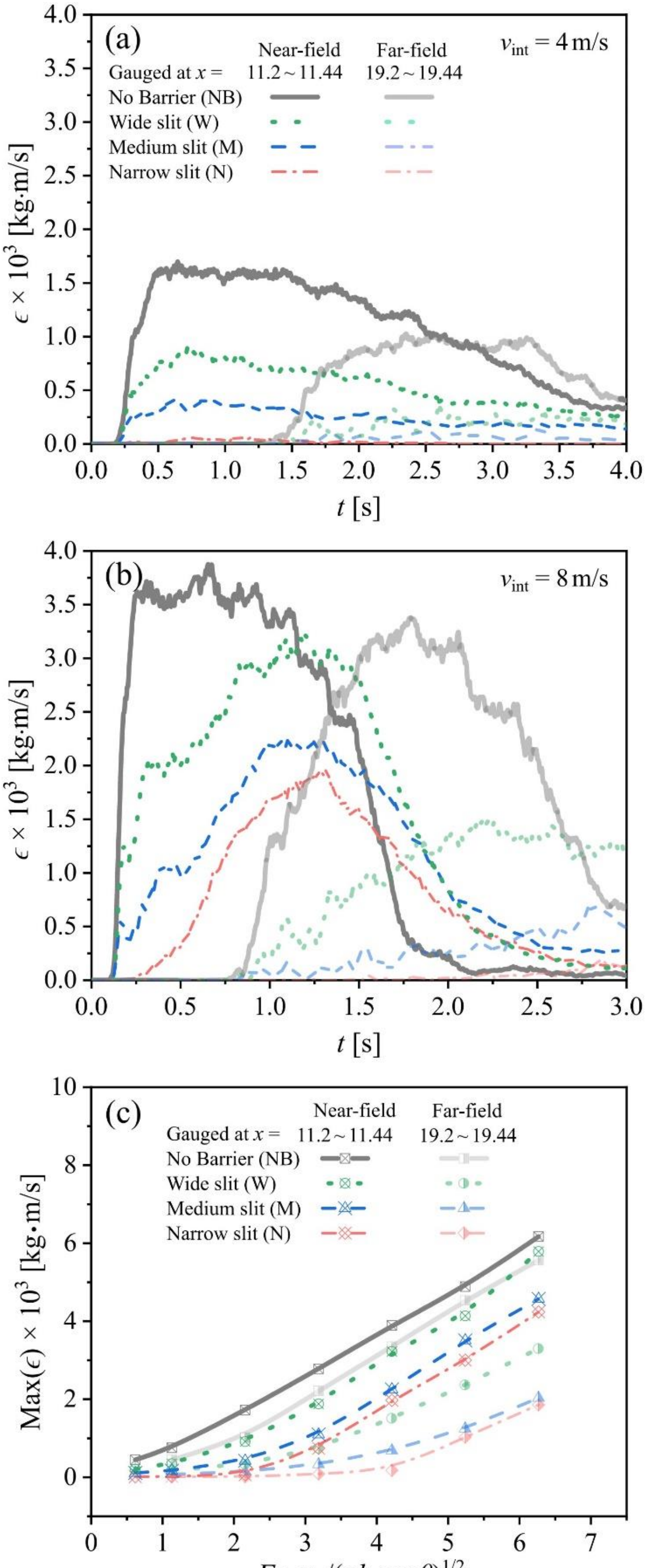

Figure A2. Time-series data of downstream momentum ϵ acquired at 11.2 m < x < 11.44 m (near-field) and 19.2 m < x < 19.44 m (far-field) in debris avalanches (a: v_{int} = 4 m/s and b: v_{int} = 8 m/s) impacting slit dams. (c) presents near- and far-field Max(ϵ) during the whole process of debris avalanches against slit dams.

References

Abbasi, N. A., Xu, X., Lucas-Borja, M. E., Dang, W., & Liu, B. (2019). The use of check dams in watershed management projects: Examples from around the world. *Science of the Total Environment*, *676*, 683-691. https://doi.org/10.1016/j.scitotenv.2019.04.249

Agliardi, F., Scuderi, M. M., Fusi, N., & Collettini, C. (2020). Slow-to-fast transition of giant creeping rockslides modulated by undrained loading in basal shear zones. *Nature Communications*, *11,* 1352. https://doi.org/10.1038/s41467-020-15093-3

Akan, A. O. (2021). *Open channel hydraulics*. Butterworth-Heinemann. pp. 233-244.

Armanini, A., & Larcher, M. (2001). Rational criterion for designing opening of slit-check dam. *Journal of Hydraulic Engineering, 127*(2), 94-104. https://doi.org/10.1061/(ASCE)0733-9429(2001)127:2(94)

Armanini, A., Rossi, G., & Larcher, M. (2020). Dynamic impact of a water and sediments surge against a rigid wall. *Journal of Hydraulic Research, 58*(2)*,* 314-325. https://doi.org/10.1080/00221686.2019.1579113

Ayat, H., Evans, J. P., Sherwood, S. C., & Soderholm, J. (2022). Intensification of subhourly heavy rainfall. *Science*, *378*(6620), 655-659. https://doi.org/10.1126/science.abn8657

Aydin, M. C., Aytemur, H. S., & Ulu, A. E. (2022). Experimental and Numerical Investigation on Hydraulic Performance of Slit-check Dams in Subcritical Flow Condition. *Water Resources Management*, 36(5), 1693-1710. https://doi.org/10.1007/s11269-022-03103-6

Baggio, T., & D'Agostino, V. (2022). Simulating the effect of check dam collapse in a debris-flow channel. *Science of The Total Environment*, *816*, 151660. https://doi.org/10.1016/j.scitotenv.2021.151660

Bernard, M., Boreggio, M., Degetto, M., & Gregoretti, C. (2019). Model-based approach for design and performance evaluation of works controlling stony debris flows with an application to a case study at Rovina di Cancia (Venetian Dolomites, Northeast Italy). *Science of The Total Environment*, *688*, 1373-1388. https://doi.org/10.1016/j.scitotenv.2019.05.468

Bozzolan, E., Holcombe, E. A., Pianosi, F., Marchesini, I., Alvioli, M., & Wagener, T. (2023). A mechanistic approach to include climate change and unplanned urban sprawl in landslide susceptibility maps. *Science of The Total Environment*, *858*, 159412. https://doi.org/10.1016/j.scitotenv.2022.159412

Cabrera, M., & Estrada, N. (2021). Is the Grain Size Distribution a Key Parameter for Explaining the Long Runout of Granular Avalanches?. *Journal of Geophysical Research: Solid Earth*, *126*(9), e2021JB022589. https://doi.org/10.1029/2021JB022589

Campisano, A., Cutore, P., & Modica, C. (2014). Improving the evaluation of slit-check dam trapping efficiency by using a 1D unsteady flow numerical model. *Journal of Hydraulic Engineering*, *140*(7), 04014024. https://doi.org/10.1061/(ASCE)HY.1943-7900.0000868

Canelas, R. B., Domínguez, J. M., Crespo, A. J. C., Gómez-Gesteira, M., & Ferreira, R. M. L. (2017). Resolved simulation of a granular-fluid flow with a coupled SPH-DCDEM model. *Journal of Hydraulic Engineering*, *143*(9), 06017012. https://doi.org/10.1061/(ASCE)HY.1943-7900.0001331

Coussot, P., Laigle, D., Arattano, M., Deganutti, A., & Marchi, L. (1998). Direct determination of rheological characteristics of debris flow. *Journal of Hydraulic engineering*, *124*(8), 865-868. https://doi.org/10.1061/(ASCE)0733-9429(1998)124:8(865)

Chiu, Y. F., Tfwala, S. S., Hsu, Y. C., Chiu, Y. Y., Lee, C. Y., & Chen, S. C. (2021). Upstream morphological effects of a sequential check dam adjustment process. *Earth Surface Processes and Landforms*, *46*(13), 2527-2539. https://doi.org/10.1002/esp.5178

Choi, C. E., Goodwin, G. R., Ng, C. W. W., Cheung, D. K. H., Kwan, J. S., & Pun, W. K. (2016). Coarse granular flow interaction with slit structures. *Géotechnique Letters*, *6*(4), 267-274. https://doi.org/10.1680/jgele.16.00103

Choi, C. E., Ng, C. W. W., Liu, H., & Wang, Y. (2020). Interaction between dry granular flow and rigid barrier with basal clearance: analytical and physical modelling. *Canadian Geotechnical Journal*, *57*(2), 236-245. https://doi.org/10.1139/cgj-2018-0622

Faug, T. (2015). Depth-averaged analytic solutions for free-surface granular flows impacting rigid walls down inclines. *Physical Review E*, *92*(6), 062310. https://doi.org/10.1103/PhysRevE.92.062310

Faug, T., Beguin, R., & Chanut, B. (2009). Mean steady granular force on a wall overflowed by free-surface gravity-driven dense flows. *Physical Review E*, *80*(2), 021305. https://doi.org/10.1103/PhysRevE.80.021305

Gong, S., Zhao, T., Zhao, J., Dai, F., & Zhou, G. G. (2021). Discrete element analysis of dry granular flow impact on slit dams. *Landslides*, 18, 1143-1152. https://doi.org/10.1007/s10346-020-01531-2

Goniva, C., Kloss, C., Deen, N. G., Kuipers, J. A., & Pirker, S. (2012). Influence of rolling friction on single spout fluidized bed simulation. *Particuology*, *10*(5), 582-591. https://doi.org/10.1016/j.partic.2012.05.002

Goodwin, G. R., & Choi, C. E. (2020). Slit structures: Fundamental mechanisms of mechanical trapping of granular flows. *Computers and Geotechnics*, *119*, 103376. https://doi.org/10.1016/j.compgeo.2019.103376

Hu, H., Zhou, G. G., Song, D., Cui, K. F. E., Huang, Y., Choi, C. E., & Chen, H. (2020). Effect of slit size on the impact load against debris-flow mitigation dams. *Engineering Geology*, *274*, 105764. https://doi.org/10.1007/s10652-021-09819-0

Huang, T., Ding, M., Gao, Z., & Téllez, R. D. (2021). Check dam storage capacity calculation based on high-resolution topogrammetry: Case study of the Cutou Gully, Wenchuan County, China. *Science of The Total Environment*, *790*, 148083. https://doi.org/10.1016/j.scitotenv.2021.148083

Hungr, O., Morgan, G. C., & Kellerhals, R. (1984). Quantitative analysis of debris torrent hazards for design of remedial measures. *Canadian Geotechnical Journal*, *21*(4), 663-677. https://doi.org/10.1139/t84-073

Iverson, R. M. (1997). The physics of debris flows. *Reviews of Geophysics*, *35*(3), 245-296. https://doi.org/10.1029/97RG00426

Iverson, R. M. (2003). The debris-flow rheology myth. *Debris-flow hazards mitigation: mechanics, prediction, and assessment*, (eds Rickenmann D. and Chen C. L.), *1*, 303-314. Rotterdam,the Netherlands: Millpress

Iverson, R. M., George, D. L., & Logan, M. (2016). Debris flow runup on vertical barriers and adverse slopes. *Journal of Geophysical Research: Earth Surface*, *121*(12), 2333-2357. https://doi.org/10.1002/2016JF003933

Iverson, R. M., Reid, M. E., Logan, M., LaHusen, R. G., Godt, J. W., & Griswold, J. P. (2011). Positive feedback and momentum growth during debris-flow entrainment of wet bed sediment. *Nature Geoscience*, *4*(2), 116–121. https://doi.org/10.1038/ngeo1040

Kaitna, R., Palucis, M. C., Yohannes, B., Hill, K. M., & Dietrich, W. E. (2016). Effects of coarse grain size distribution and fine particle content on pore fluid pressure and shear behavior in experimental debris flows. *Journal of Geophysical Research: Earth Surface*, *121*(2), 415-441. https://doi.org/10.1002/2015JF003725

Kaitna, R., Prenner, D., Switanek, M., Maraun, D., Stoffel, M., & Hrachowitz, M. (2023). Changes of hydro-meteorological trigger conditions for debris flows in a future alpine climate. *Science of the Total Environment*, *872*, 162227. https://doi.org/10.1016/j.scitotenv.2023.162227

Kong, Y., & Guan, M. F. (2023): Dataset and supplementary movies for geophysical mass flows against slit dams. [Dataset]. *HKU Data Repository*. https://doi.org/10.25442/hku.22208008.v1

Kong, Y., Guan, M. F., Li, X. Y., Zhao, J. D., & Yan, H. C. (2022a). How Flexible, Slit and Rigid Barriers Mitigate Two-phase Geophysical Mass Flows: A Numerical Appraisal. *Journal of Geophysical Research: Earth Surface*, 127(6), e2021JF006587. https://doi.org/10.1029/2021JF006587

Kong, Y., Guan, M. F., Li, X. Y., Zhao, J. D., & Yan, H. C. (2022b). Bi-linear Laws Govern the Impacts of Debris Flows, Debris Avalanches and Rock Avalanches on Flexible Barrier. *Journal of Geophysical Research: Earth Surface*, 127(11), e2022JF006870. https://doi.org/10.1029/2022JF006870

Kong, Y., Li, X. Y., & Zhao, J. D. (2021a). Quantifying the transition of impact mechanisms of geophysical flows against flexible barrier. *Engineering Geology*, *289*, 106188. https://doi.org/10.1016/j.enggeo.2021.106188

Kong, Y., Li, X., Zhao, J., & Guan, M. (2023). Load deflection of flexible ring net barrier in resisting debris flows. *Géotechnique*, 1-13, e-First. https://doi.org/10.1680/jgeot.22.00135

Kong, Y., Zhao, J. D., & Li, X. Y. (2021b). Hydrodynamic dead zone in multiphase geophysical flows impacting a rigid obstacle. *Powder Technology*, *386*, 335-349. https://doi.org/10.1016/j.powtec.2021.03.053

Kostynick, R., Matinpour, H., Pradeep, S., Haber, S., Sauret, A., Meiburg, E., ... & Jerolmack, D. (2022). Rheology of debris flow materials is controlled by the distance from jamming. *Proceedings of the National Academy of Sciences*, *119*(44), e2209109119. https://doi.org/10.1073/pnas.2209109119

Li, D., Lu, X., Walling, D. E., Zhang, T., Steiner, J. F., Wasson, R. J., ... & Bolch, T. (2022). High Mountain Asia hydropower systems threatened by climate-driven landscape instability. *Nature Geoscience*, *15*, 520-530. https://doi.org/10.1038/s41561-022-00953-y

Li, X., Yan, Q., Zhao, S., Luo, Y., Wu, Y., & Wang, D. (2020). Investigation of influence of baffles on landslide debris mobility by 3D material point method. *Landslides*, *17*, 1129-1143. https://doi.org/10.1007/s10346-020-01346-1

Li, X., Zhao, J., & Soga, K. (2021). A new physically based impact model for debris flow. *Géotechnique*, *71*(8), 674–685. https://doi.org/10.1680/jgeot.18.P.365

Lucas-Borja, M. E., Piton, G., Nichols, M., Castillo, C., Yang, Y., & Zema, D. A. (2019). The use of check dams for soil restoration at watershed level: A century of history and perspectives. *Science of The Total Environment*, *692*, 37-38. https://doi.org/10.1016/j.scitotenv.2019.07.248

Lucas-Borja, M. E., Piton, G., Yu, Y., Castillo, C., & Zema, D. A. (2021). Check dams worldwide: Objectives, functions, effectiveness and undesired effects. *Catena*, *204*, 105390. https://doi.org/10.1016/j.catena.2021.105390

Marchelli, M., Leonardi, A., Pirulli, M., & Scavia, C. (2020). On the efficiency of slit-check dams in retaining granular flows. *Géotechnique*, *70*(3), 226-237. https://doi.org/10.1680/jgeot.18.P.044

Marchi, L., Comiti, F., Crema, S., & Cavalli, M. (2019). Channel control works and sediment connectivity in the European Alps. *Science of the Total Environment*, *668*, 389-399. https://doi.org/10.1016/j.scitotenv.2019.02.416

Mühlburger, R. (2015). The bed load retention barrier on the Erlbach in Abfaltersbach. See https://www.osttirol-heute.at/menschen/neben (accessed 05/02/2023)

Ng, C. W. W., Bhatta, A., Choi, C. E., Poudyal, S., Liu, H. M., Cheung, R. W. M., & Kwan, J. S. H. (2022a). Effects of debris flow rheology on overflow and impact dynamics against dual-rigid barriers. *Géotechnique*, 1-14, e-First. https://doi.org/10.1680/jgeot.21.00226

Ng, C. W. W., Choi, C. E., Goodwin, G. R., & Cheung, W. W. (2017). Interaction between dry granular flow and deflectors. *Landslides*, *14*(4), 1375-1387. https://doi.org/10.1007/s10346-016-0794-3

Ng, C. W. W., Majeed, U., & Choi, C. E. (2022b). Effects of solid fraction of saturated granular flows on overflow and landing mechanisms of rigid barriers. *Géotechnique*, 1-15, e-First. https://doi.org/10.1680/jgeot.21.00170

Otsubo, M., O'Sullivan, C., Hanley, K. J., & Sim, W. W. (2017). The influence of particle surface roughness on elastic stiffness and dynamic response. *Géotechnique*, *67*(5), 452-459. https://doi.org/10.1680/jgeot.16.P.050

Piton, G., Carladous, S., Recking, A., Tacnet, J. M., Liébault, F., Kuss, D., ... & Marco, O. (2017). Why do we build check dams in Alpine streams? An historical perspective from the French experience. *Earth Surface Processes and Landforms*, *42*(1), 91-108. https://doi.org/10.1002/esp.3967

Piton, G., Goodwin, G. R., Mark, E., & Strouth, A. (2022) Debris flows, boulders and constrictions: a simple framework for modeling jamming, and its consequences on outflow. *Journal of Geophysical Research: Earth Surface*, *127*(5), e2021JF006447. https://doi.org/10.1029/2021JF006447

Piton, G., Horiguchi, T., Marchal, L., & Lambert, S. (2020). Open check dams and large wood: head losses and release conditions. *Natural Hazards and Earth System Sciences*, *20*(12), 3293-3314. https://doi.org/10.5194/nhess-20-3293-2020, 2020

Piton, G., & Recking, A. (2016). Design of sediment traps with open check dams. I: hydraulic and deposition processes. *Journal of Hydraulic Engineering*, *142*(2), 04015045. https://doi.org/10.1061/(ASCE)HY.1943-7900.0001048

Pudasaini, S. P., & Fischer, J. T. (2020). A mechanical model for phase separation in debris flow. *International Journal of Multiphase Flow*, *129*, 103292. https://doi.org/10.1016/j.ijmultiphaseflow.2020.103292

Pudasaini, S. P., & Krautblatter, M. (2021). The mechanics of landslide mobility with erosion. *Nature Communications*, *12*, 6793. https://doi.org/10.1038/s41467-021-26959-5

Pudasaini, S. P., & Mergili, M. (2019). A multi-phase mass flow model. *Journal of Geophysical Research: Earth Surface*, *124*(12), 2920-2942. https://doi.org/10.1029/2019JF005204

Remaître, A., Malet, J. P., Maquaire, O., Ancey, C., & Locat, J. (2005). Flow behaviour and runout modelling of a complex debris flow in a clay-shale basin. *Earth Surface Processes and Landforms*, *30*(4), 479-488. https://doi.org/10.1002/esp.1162

Rossi, G., & Armanini, A. (2019). Impact force of a surge of water and sediments mixtures against slit check dams. *Science of The Total Environment*, *683*, 351-359. https://doi.org/10.1016/j.scitotenv.2019.05.124

Shan, T., & Zhao, J. (2014). A coupled CFD-DEM analysis of granular flow impacting on a water reservoir. *Acta Mechanica*, *225*, 2449-2470. https://doi.org/10.1007/s00707-014-1119-z

Song, D., Chen, X., Zhou, G. G., Lu, X., Cheng, G., & Chen, Q. (2021a). Impact dynamics of debris flow against rigid obstacle in laboratory experiments. *Engineering Geology*, *291*, 106211. https://doi.org/10.1016/j.enggeo.2021.106211

Song, D., Choi, C. E., Ng, C. W. W., & Zhou, G. G. D. (2018). Geophysical flows impacting a flexible barrier: effects of solid-fluid interaction. *Landslides*, *15*, 99-110. https://doi.org/10.1007/s10346-017-0856-1

Song, D., Zhou, G. G., Chen, X. Q., Li, J., Wang, A., Peng, P., & Xue, K. X. (2021b). General equations for landslide-debris impact and their application to debris-flow flexible barrier. *Engineering Geology*, *288*, 106154. https://doi.org/10.1016/j.enggeo.2021.106154 von Boetticher, A., Turowski, J. M., McArdell, B. W., Rickenmann, D., & Kirchner, J. W. (2016). DebrisInterMixing-2.3: a finite volume solver for three-dimensional debris-flow simulations with two calibration parameters–Part 1: Model description. *Geoscientific Model Development*, *9*(9), 2909-2923. https://doi.org/10.5194/gmd-9-2909-2016

Wang, D., Wang, X., Chen, X., Lian, B., & Wang, J. (2022). Analysis of factors influencing the large wood transport and block-outburst in debris flow based on physical model experiment. *Geomorphology*, *398*, 108054. https://doi.org/10.1016/j.geomorph.2021.108054

Wu, Y., Wang, D., Li, P., & Niu, Z. (2022). Experimental investigation of dry granular flows down an inclined channel against a wall-like obstacle of limited width. *Acta Geotechnica*, 1-14. https://doi.org/10.1007/s11440-022-01714-2

Yang, E., Bui, H. H., Nguyen, G. D., Choi, C. E., Ng, C. W., De Sterck, H., & Bouazza, A. (2021). Numerical investigation of the mechanism of granular flow impact on rigid control structures. *Acta Geotechnica*, *16*, 2505-2527. https://doi.org/10.1007/s11440-021-01162-4

Yin J., Gao Y., Chen R., Yu D., Wilby R., Wright N., Ge Y., Bricker J., Gong H., & Guan M. (2023) Flash floods: why are more of them devastating the world's driest regions? *Nature*, *615*, 212-215. https://doi.org/10.1038/d41586-023-00626-9

Yu, T., & Zhao, J. (2022). Quantitative simulation of selective laser melting of metals enabled by new high-fidelity multiphase, multiphysics computational tool. *Computer Methods in Applied Mechanics and Engineering*, *399*, 115422. https://doi.org/10.1016/j.cma.2022.115422

Zhao, J., & Shan, T. (2013). Coupled CFD–DEM simulation of fluid-particle interaction in geomechanics. *Powder Technology*, *239*, 248–258. https://doi.org/10.1016/j.powtec.2013.02.003

Zhang, B., & Huang, Y. (2022). Impact behavior of dry granular flow against baffle structure: Coupled effect of Froude and particle characteristics. *Géotechnique*, 1-12, e-First. https://doi.org/10.1680/jgeot.21.00360

Zhang, S., Wang, B., Zhang, L., Lacasse, S., Nadim, F., & Chen, Y. (2023). Increased human risk caused by cascading hazards–A framework. *Science of the Total Environment, 857,* 159308. https://doi.org/10.1016/j.scitotenv.2022.159308

Zhou, G. G., Du, J., Song, D., Choi, C. E., Hu, H. S., & Jiang, C. (2020). Numerical study of granular debris flow run-up against slit dams by discrete element method. *Landslides*, *17*(3), 585-595. https://doi.org/10.1007/s10346-019-01287-4

Zhou, G. G., Hu, H. S., Song, D., Zhao, T., & Chen, X. Q. (2019). Experimental study on the regulation function of slit dam against debris flows. *Landslides*, *16*(1), 75-90. https://doi.org/10.1007/s10346-018-1065-2

Zhou, Z. Y., Kuang, S. B., Chu, K. W., & Yu, A. B. (2010). Discrete particle simulation of particle-fluid flow: model formulations and their applicability. *Journal of Fluid Mechanics*, *661*, 482-510. https://doi.org/10.1017/S002211201000306X

Highlights

- We present hydro-mechanical simulations of geophysical flows against slit dams
- Impact-induced jammed and mobilized domains and three typical traps are revealed
- Flow properties and dam configurations are quantitatively linked to design indices
- Spillway widths govern trapping patterns, while flow properties drive overspilling
- We offer a unique physics-based dataset to aid demand-oriented design of slit dams

Science of The Total Environment

Supporting Information for

Hydro-mechanical Simulations Aid Demand-oriented Design of Slit Dams for Controlling Debris Flows, Debris Avalanches and Rock Avalanches

Yong Kong[1] and Mingfu Guan[1†]

[1] Department of Civil Engineering, The University of Hong Kong, Hong Kong SAR, China.

[†] Corresponding author: Mingfu Guan (mfguan@hku.hk)

Contents of this file

Text S1 to S6

Figures S1 to S5

Additional supporting information (*Files uploaded separately*)

Movie S1. Debris flow impacting a slit dam with a medium-sized spillway

Movie S2. Debris flows and rock avalanches impacting slit dams: wet versus dry, slow versus fast, and narrow versus wide

Tables 4, 5, 6, 8, and A2

Introduction

This support information contains several components that support the main paper. Text S1 provides field observations of slit-check dams for controlling geophysical mass flows. Text S2, Text S3, Text S4, and Text S5 discuss the key ingredients of the CFD-DEM coupling method, including fluid-solid interactions, particle-particle and particle-wall contacts, the three-phase VOF method, and coupling procedures. Text S6 provides a comparison of key flow-dam interactions between experimental observations and numerical predictions for mixture flow against slit dams. The supplementary movie S1 (presented in Figure 2b) demonstrates a typical debris flow impacting a slit dam with v_{int} = 8 m/s. The supplementary movie S2 (presented in Figure 3) compares debris flows and rock avalanches with slow and fast impact dynamics impacting slit dams with different spillways. The two videos can be archived at https://doi.org/10.25442/hku.22208008.v1 (Kong and Guan, 2023). Tables 4, 5, 6, 8, and A2 contain the dataset for plotting Figures 4, 5, 6, 8, and A2 in the paper, and can be permanently archived at Kong and Guan (2023).

Text S1. Slit-check dams for controlling geophysical mass flows

Figure S1 provides readers with an intuitive understanding of real-world slit dams used for arresting or controlling natural geophysical mass flows, such as debris flows, debris avalanches, muddy flows, and debris floods, which are typically composed of solid particles and viscous slurry. The size of slit dams can vary significantly, ranging from large (Figures S1b and S1c) to small (Figures S1d and S1e). The spillway can be multiple (Figure S1b) or single (Figures S1c, S1d, and S1e). Moreover, slit dams are used for diverse objectives, including community and infrastructure protection (Figures S1a and S1b), erosion and torrent control (Figures S1c and S1e), moderate water and sediment flows (Figures S1a, S1c, and S1d), and retaining large boulders and woods (Figures S1a, S1b, and S1c). Notably, the overspilling dynamics should be a critical design consideration for slit dams constructed near roadways (Figure S1d).

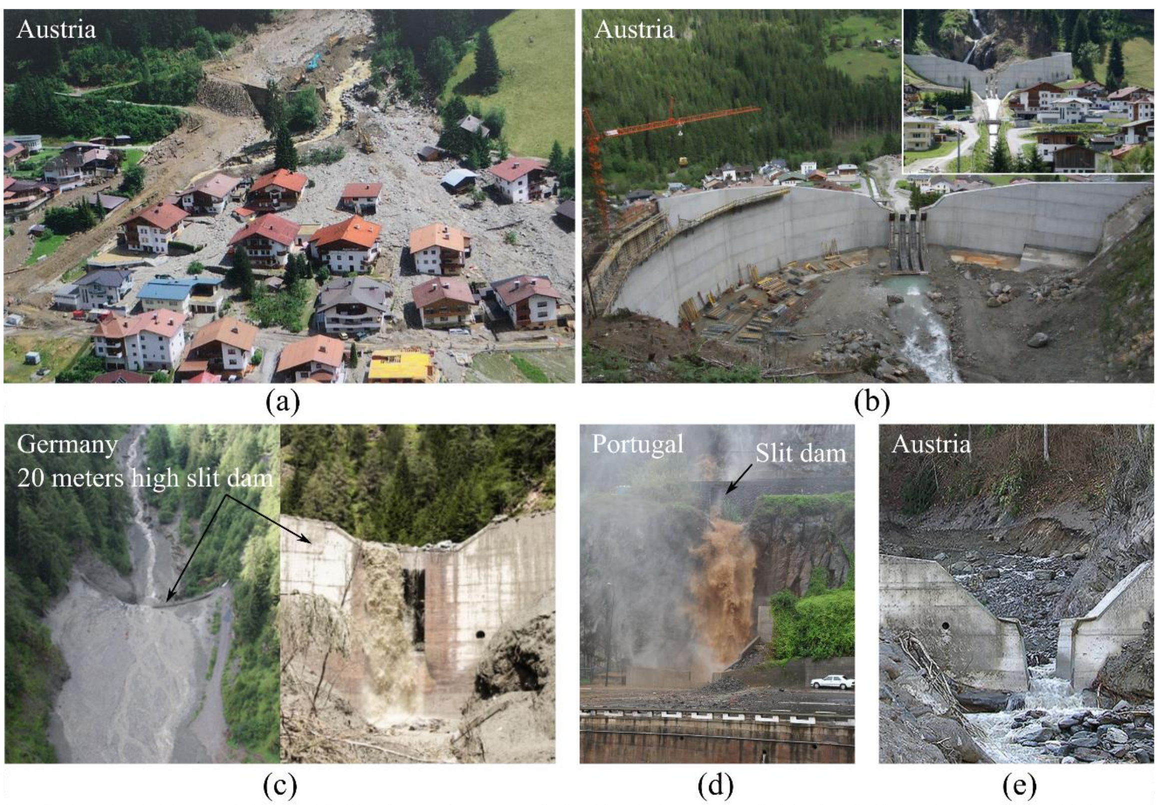

Figure S1. Field photos showing slit dams constructed for controlling geophysical mass flows

Notes: Photos *a* and *b* are modified from https://www.meinbezirk.at/landeck/c-lokales/schallerbach-neuer-schutzdamm-ist-fertig_a1761095; Photo *c* is modified from https://www.dolomitenstadt.at/2012/08/07/virger-mure-richtete-millionenschaden-an/; Photo *d* is modified from https://www.tsf.pt/portugal/sociedade/dez-anos-apos-a-tragedia-a-madeira-estamais-bem-preparada-para-enfrentar-catastrofes-11837025.html; Photo *e* is modified from https://kaernten.orf.at/v2/news/stories/2946252.

Test S2. Fluid-solid interactions

This study incorporates fluid-solid interactions by exchanging interaction forces $\boldsymbol{F}^{\mathrm{f}}$ in Eq. (1) in Sect. 2.1 between the computational fluid dynamics (CFD) and discrete element method (DEM) computations. Two open-source software packages, namely, OpenFoam (https://www.openfoam.com) and LIGGGHTS (https://www.lammps.org), are used for the CFD and DEM engines, respectively. The coupling between the CFD and DEM is based on an interface program CFDEM (https://www.cfdem.com). The coupled CFD-DEM modeling of multiphase geophysical flows was developed and validated in the previous work (Kong, 2020; Kong et al., 2021, 2022, 2023; Zhao and Shan, 2013). In this study, four interaction forces are considered, including drag force $\boldsymbol{F}^{\mathrm{d}}$, buoyancy force $\boldsymbol{F}^{\mathrm{b}}$, viscous force $\boldsymbol{F}^{\mathrm{v}}$ and virtual mass force $\boldsymbol{F}^{\mathrm{vm}}$:

$$\boldsymbol{F}^{\mathrm{f}} = \boldsymbol{F}^{\mathrm{d}} + \boldsymbol{F}^{\mathrm{b}} + \boldsymbol{F}^{\mathrm{v}} + \boldsymbol{F}^{\mathrm{vm}} \tag{S1}$$

The drag force proposed by Di Felice (1994) is adopted:

$$\begin{cases} \boldsymbol{F}^{\mathrm{d}} = \frac{1}{2} C_{\mathrm{d}} \pi \rho_{\mathrm{f}} r_i^2 \left(\boldsymbol{U}^{\mathrm{f}} - \boldsymbol{U}^{\mathrm{p}}\right) \left|\boldsymbol{U}^{\mathrm{f}} - \boldsymbol{U}^{\mathrm{p}}\right| \varepsilon^{1-\chi}, \\ C_{\mathrm{d}} = \left(0.63 + \frac{4.8}{\sqrt{Re_{\mathrm{p}}}}\right)^2, \\ Re_{\mathrm{p}} = \frac{2\varepsilon_{\mathrm{f}} \rho_{\mathrm{f}} r_i \left|\boldsymbol{U}^{\mathrm{f}} - \boldsymbol{U}^{\mathrm{p}}\right|}{\mu}, \\ \chi = 3.7 - 0.65 exp\left[-\frac{(1.5 - log_{10} Re_{\mathrm{p}})^2}{2}\right] \end{cases} \tag{S2}$$

where C_{d} is the particle-fluid drag coefficient depending on the particle Reynolds number Re_{p}. $\varepsilon^{1-\chi}$ denotes a corrective function that accounts for the effect of other particles in the system on the drag force of the considered particle i.

The average density based buoyancy force acting on the considered particle i with radius r_i is given by (Zhao and Shan, 2013):

$$\boldsymbol{F}^{b} = \frac{4}{3} \pi \rho_{\mathrm{f}} r_i^3 \mathbf{g} \tag{S3}$$

The viscous force acting on particle i with volume V_i^{p} is induced by the deviatoric stress tensor and is defined by Zhou et al. (2010):

$$\boldsymbol{F}^{v} = -(\nabla \cdot \boldsymbol{\tau}) V_i^{\mathrm{p}} \tag{S4}$$

When a particle accelerates or decelerates in a fluid, it needs to deflect a certain volume of the surrounding fluid to move through, generating extra virtual inertia in the system. The virtual mass force is an interaction force to account for this effect and is defined as (Shan and Zhao, 2014):

$$\boldsymbol{F}^{\mathrm{vm}} = C_{\mathrm{vm}}\rho_{\mathrm{f}}V_i^{\mathrm{p}}(\dot{\boldsymbol{U}}_i^{\mathrm{p}} - \dot{\boldsymbol{U}}^{\mathrm{f}})/ \quad \text{(S5)}$$

where the virtual mass coefficient C_{vm}= 2.1 - 0.132/(0.12 + A_c), $A_c = \left(\boldsymbol{U}^{\mathrm{p}} - \boldsymbol{U}^{\mathrm{f}}\right)^2/[(\dot{\boldsymbol{U}}_i^{\mathrm{p}} - \dot{\boldsymbol{U}}^{\mathrm{f}})2r_i]$. $\dot{\boldsymbol{U}}_i^{\mathrm{p}}$ and $\dot{\boldsymbol{U}}^{\mathrm{f}}$ are the accelerations of the particle i and the fluid in a cell, respectively.

More details of the fluid-solid interaction forces can be referred to literature (Di Felice, 1994; Zhao and Shan, 2013; Zhou et al., 2010).

Text S3. Particle-particle and particle-wall contacts

Figure S2a illustrates that the two particles, i and j, are in contact. The contact forces include normal force and tangential force, and a friction slider. Specifically, the contact force $\boldsymbol{F}_{ij}^{\mathrm{c}}$ in Eq. (1) in Sect. 2.1 is calculated by the Hertzian-Mindlin contact law (Kloss et al., 2012):

$$\boldsymbol{F}_{ij}^{\mathrm{c}} = (k_{\mathrm{n}}\delta_{ij}^{\boldsymbol{n}} - c_{\mathrm{n}}\mathrm{v}_{ij}^{\boldsymbol{n}}) + [(\boldsymbol{F}_{\mathrm{spring}}^{\mathrm{s0}} + k_{\mathrm{s}}\Delta\delta_{ij}^{\boldsymbol{t}}) - c_{\mathrm{s}}\mathrm{v}_{ij}^{\boldsymbol{t}}] \quad \text{(S6)}$$

where the normal and tangential stiffness: k_n and k_s, the damping coefficients for normal and tangential contacts: c_n and c_s, and the friction coefficient μ are illustrated in Figure S2a. The terms on the right side refer to the normal spring force, the normal damping force, the shear spring force and the shear damping force, respectively. The total tangential force is the sum of shear spring force and shear damping force, denoted by the term in the square bracket. It increases until the shear spring force $\boldsymbol{F}_{\mathrm{spring}}^{\mathrm{s}}$ (i.e. $\boldsymbol{F}_{\mathrm{spring}}^{\mathrm{s0}} + k_{\mathrm{s}}\Delta\delta_{ij}^{\boldsymbol{t}}$) reaches $\mu\boldsymbol{F}_{\mathrm{n}}$. $\boldsymbol{F}_{\mathrm{spring}}^{\mathrm{s0}}$ is the initial tangential spring force at the previous time step. $\boldsymbol{F}_{\mathrm{n}}$ is the total normal force in the first parenthesis. The shear spring force is then held at $\boldsymbol{F}_{\mathrm{spring}}^{\mathrm{s}} = \mu\boldsymbol{F}_{\mathrm{n}}$ until the particles lost contact. $\delta_{ij}^{\boldsymbol{n}}$ is the overlap distance in the normal direction and $\Delta\delta_{ij}^{\boldsymbol{t}}$ denotes the incremental tangential displacement.$\mathrm{v}_{ij}^{\boldsymbol{n}}$ and $\mathrm{v}_{ij}^{\boldsymbol{t}}$ are the normal and tangential components of the relative velocity of the overlapped two particles i and j. The normal and tangential stiffness (k_{n} and k_{s}) as well as the damping coefficients (c_{n} and c_{s}) can be calculated by:

$$k_{\mathrm{n}} = \frac{3}{4}E^*\sqrt{r^*\delta_{ij}^{\boldsymbol{n}}} \quad \text{(S7)}$$

$$k_s = 8G^* \sqrt{r^* \delta_{ij}^{\boldsymbol{n}}} \tag{S8}$$

$$c_n = -2\sqrt{\frac{5}{6}}\beta\sqrt{m^* S_n} \tag{S9}$$

$$c_s = -2\sqrt{\frac{5}{6}}\beta\sqrt{m^* S_t} \tag{S10}$$

where $\frac{1}{E^*} = \frac{(1-\vartheta_i^2)}{E_i} + \frac{(1-\vartheta_j^2)}{E_j}$; $\frac{1}{G^*} = \frac{2(2-\vartheta_i)(1+\vartheta_i)}{E_i} + \frac{2(2-\vartheta_j)(1+\vartheta_j)}{E_j}$; $\frac{1}{r^*} = \frac{1}{r_i} + \frac{1}{r_j}$; $\frac{1}{m^*} = \frac{1}{m_i} + \frac{1}{m_j}$; $S_n = 2E^*\sqrt{R^*\delta_{ij}^n}$; $S_t = 8G^*\sqrt{R^*\delta_{ij}^n}$; $\beta = \frac{ln(e)}{\sqrt{ln^2(e)+\pi^2}}$. E_i and E_i are Young's moduli of two contacting particles i and j. ϑ_i and ϑ_j are the Poisson's ratios of particles i and j. r_i and r_j are the radii of the contacting particles. m_i and m_j are the masses of the contacting particles. e is the coefficient of restitution. Moreover, Figure S2b illustrates that the contact behavior between a particle i and a wall follows the same law described above, where the wall is regarded as a particle with infinite radius and mass.

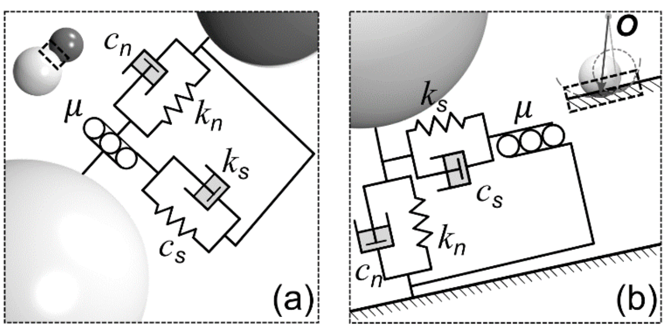

Figure S2. Schematic illustrations of the Hertzian-Mindlin contact law. The key model parameters include the normal and tangential stiffness ($\boldsymbol{k_n}$ and $\boldsymbol{k_s}$), the damping coefficients for normal and tangential contacts ($\boldsymbol{c_n}$ and $\boldsymbol{c_s}$), and friction coefficient $\boldsymbol{\mu}$. (a) and (b) specifically illustrate these parameters for interparticle and particle-wall interactions, respectively. Note: this figure is from Kong (2020).

Text S4. Three-phase VOF method

Figure S3 depicts the implementation of the three-phase volume of fluid (VOF) method. The void fraction or porosity $\boldsymbol{\varepsilon_f}$ in Eqs. (3, 4) in Sect. 2.1 is calculated by $\boldsymbol{\varepsilon_f} = V_{void}/V_c = 1 - V_p/V_c$, where V_{void}, V_p and V_c represent the void volume, particle(s) volume, and total volume of a cell, respectively, as shown in Figure S3a. The average fluid density ρ_f and viscosity μ_f of immiscible liquid and gas in a cell needed in the momentum equation are calculated according to:

$$\rho_\mathrm{f} = \alpha_l \rho_l + (1 - \alpha_l)\rho_\mathrm{g} \tag{S11}$$

$$\mu_\mathrm{f} = \alpha_l \mu_l + (1 - \alpha_l)\mu_\mathrm{g} \tag{S12}$$

where ρ_f, ρ_g, μ_f and $\mu_\mathrm{g}$are liquid phase density, gas-phase density, liquid phase viscosity and gas-phase viscosity, respectively. $\alpha_l = V_l/V_\mathrm{void} = 1 - V_\mathrm{g}/V_\mathrm{void}$ denotes the nominal volume fraction of liquid phase in a cell, where $V_l + V_\mathrm{g} = V_\mathrm{void}$. Specifically, the case of 1 < α_l < 0 represents a cell with void occupied by liquid and gas, as shown in Figure S3a. If $\alpha_l = 0$, the void of a cell will be full of liquid, and if $\alpha_l = 1$, the void is filled by gas. Besides, the nominal volume fraction α_l and porosity ε_f of a cell will update when volume flux through the interface of neighboring cells during the time interval Δt. As shown in Figure S3b. the nominal volume fraction α_l is updated from α_l^t to $\alpha_l^{t+\Delta t}$ owing to the varied void fraction from ε_f^t to $\varepsilon_f^{t+\Delta t}$, where i and $i+1$ are neighboring cell centroids.

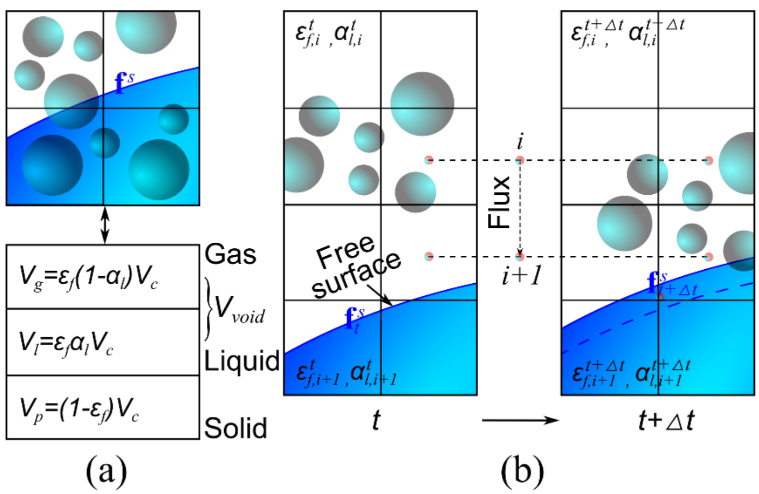

Figure S3. Illustrations of the three-phase VOF method. (a): Phase fraction. (b): Volume flux during $\Delta \boldsymbol{t}$ and corresponding updates of the free surface, nominal volume fraction $\boldsymbol{\alpha_l}$ and porosity $\boldsymbol{\varepsilon_\mathrm{f}}$ of a cell. Note: this figure is from Kong (2020).

Furthermore, the update of the air-liquid interface determined by phase fractions occurs (i.e., from dotted blue interface to solid blue interface, shown in Figure S3b), even before the particle(s) reach the free surface. This is due to the cell-based discretization in the VOF method. Similarly, the exact position of the air-liquid interface is determined algebraically from phase fractions, and the phase fraction distribution is smeared over a few fluid cells. This mixture VOF method saves computational costs compared to the more sophisticated drag-force-based multiphase models (von Boetticher et al., 2016). To improve the accuracy of predictions, the divided porosity calculation method, previously described by Zhao and Shan (2013), is used, which involves dividing edge particles into different cells.

Text S5. CFD-DEM Coupling Procedures

The two-way coupling between the discrete element method (DEM) and computational fluid dynamics (CFD) computations follows a sequential iterative procedure (Figure S4). At each time step, the DEM provides information such as particle velocities and positions. The positions of all particles are then matched with fluid cells to calculate relevant information, such as porosity and the assembled momentum source term $\boldsymbol{f}^{\mathrm{p}} = \frac{1}{v_{\mathrm{c}}}\sum_{i=1}^{n_{\mathrm{c}}} \boldsymbol{F}_i^{\mathrm{f}}$ of each cell. Once all state variables, such as averaged velocity and pressure, are resolved for each fluid cell by the CFD, particle-fluid interaction forces acting on the centroid of each particle are updated and transferred back to the DEM to solve the particle system for the next time step. A more detailed description of the solution procedures can be found in Zhao and Shan (2013).

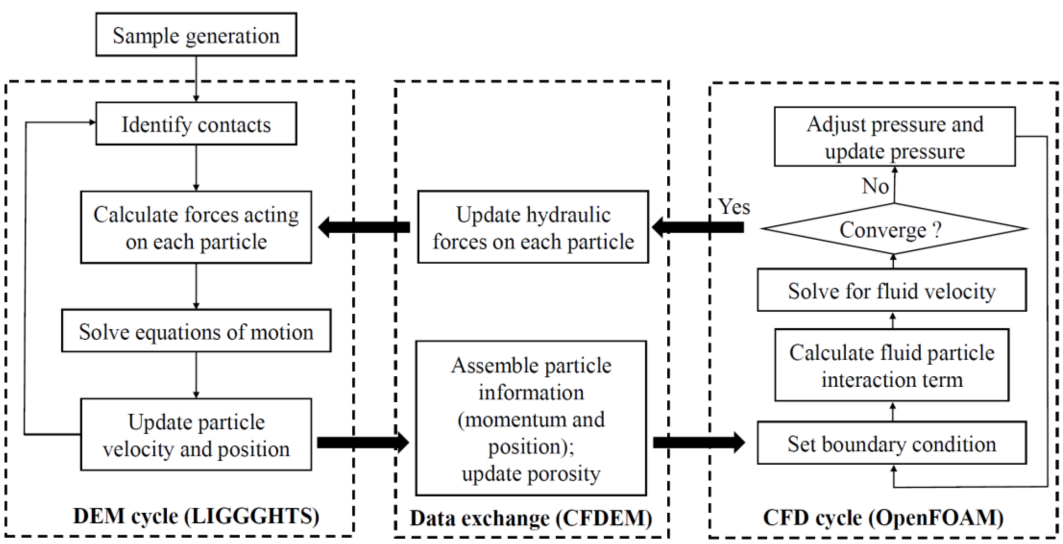

Figure S4. Flow chart illustrating the discrete element method (DEM) cycle, the computational fluid dynamics (CFD) cycle, and the coupling schemes between them, as utilized in the coupled CFD-DEM approach. Note: this figure is from Kong (2020).

Text S6. Comparison of Key Flow-dam Interactions

Observations from both field studies and experiments are crucial for understanding the complex interactions between geophysical flows and slit dams. The authors' prior research has presented benchmarking tests of geophysical flows against rigid, slit, and flexible barriers (Kong et al., 2021; 2022). This paper qualitatively compares the jet impact mode for mixture flows against single-spillway slit dams between the experimental observation by Rossi and Armanini (2019) and the numerical prediction (see Figure 2b in Sect. 2.2). This supporting material also presents a qualitative comparison between numerical predictions, using a CFD-DEM coupled model, and experimental observations (Hu et al., 2020) on the key flow-barrier interactions for mixture flows impacting multi-spillway slit dams (Figure S5). The critical conditions for the small-scale flume test conducted by Hu et al. (2020) include *Fr* = 3.65, relative post spacing $b/d_{\max}$ = 1.8, and flow-dam height ratio = 0.08. Accordingly, the critical pre-impact conditions for the numerical case are *Fr* = 3.9, relative post spacing $b/d_{\max}$ = 1.875, and flow-dam height ratio = 0.33. Figure S5 demonstrates that the numerical predictions of the key characteristics of flow-barrier interactions, such as evolving dynamics of impinging flows, jet-like overspilling flows, outlet flows, and the formation of dead zones, agree well with experimental observations under the Froude similarity. The differences between experimental observations and numerical results may be due to the different flow-dam height ratios (i.e., 0.08 in Hu et al., 2020, versus 0.33 in the numerical case).

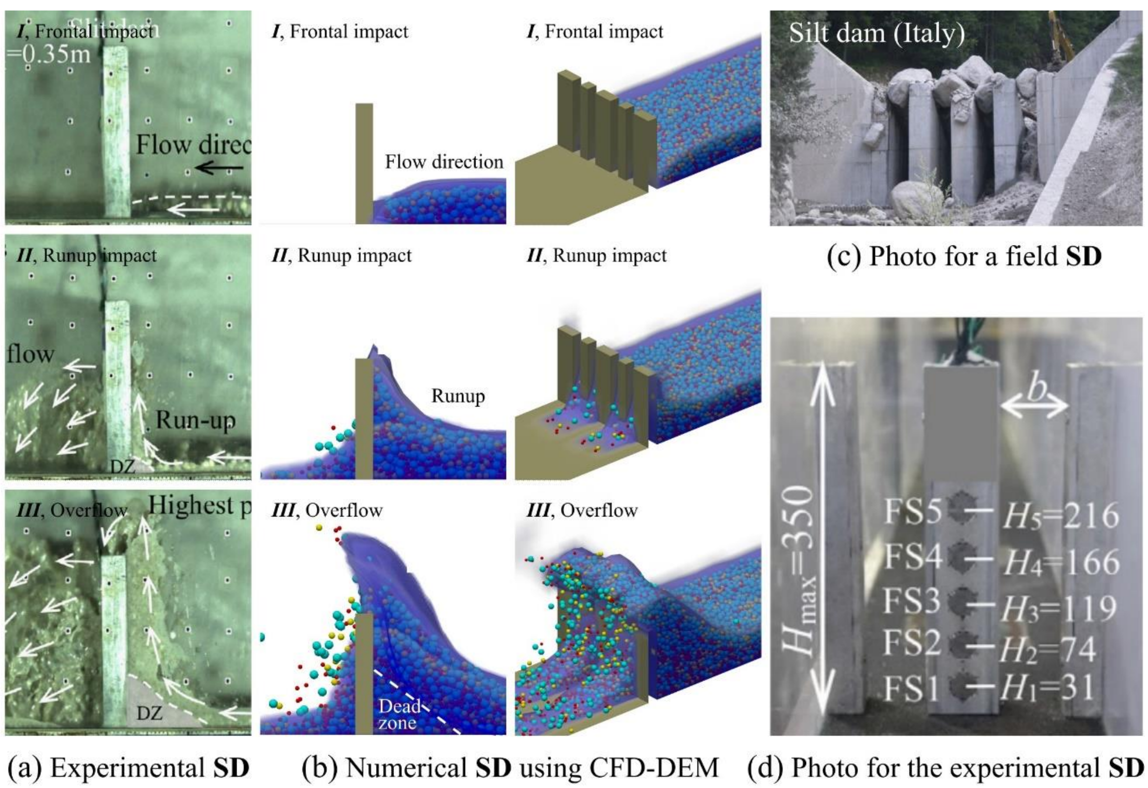

Figure S5. Comparisons of key flow-dam interactions for mixture flows against multi-spillway slit dams between (a) small-scale flume test observations (Hu et al., 2020) and (b) the numerical predictions using CFD-DEM coupled model. (c) shows a typical multi-spillway slit dam in Italy (photo from Marchi et al., 2019). (d) displays the multi-spillway slit dam used in the experiment by Hu et al. (2020).

References

Di Felice, R. (1994). The voidage function for fluid-particle interaction systems. *International Journal of Multiphase Flow*, *20*(1), 153–159. https://doi.org/10.1016/0301-9322(94)90011-6

Hu, H., Zhou, G. G., Song, D., Cui, K. F. E., Huang, Y., Choi, C. E., & Chen, H. (2020). Effect of slit size on the impact load against debris-flow mitigation dams. *Engineering Geology*, *274*, 105764. https://doi.org/10.1016/j.enggeo.2020.105764

Kloss, C., Goniva, C., Hager, A., Amberger, S., & Pirker, S. (2012). Models, algorithms and validation for opensource DEM and CFD–DEM. *Progress in Computational Fluid Dynamics, an International Journal*, *12*(2-3), 140-152. https://doi.org/10.1504/PCFD.2012.047457

Kong Y. (2020). Computational modeling and analysis of multiphase geophysical flows interacting with resisting structures. *Ph.D. Thesis*. The Hong Kong University of Science and Technology, Hong Kong, China

Kong, Y., & Guan, M. F. (2023): Dataset and supplementary movies for geophysical mass flows against slit dams. [Dataset]. *HKU Data Repository*. https://doi.org/10.25442/hku.22208008.v1

Kong, Y., Guan, M. F., Li, X. Y., Zhao, J. D., & Yan, H. C. (2022). How Flexible, Slit and Rigid Barriers Mitigate Two-phase Geophysical Mass Flows: A Numerical Appraisal. *Journal of Geophysical Research: Earth Surface*, 127(6), e2021JF006587. https://doi.org/10.1029/2021JF006587

Kong, Y., Li, X., Zhao, J., & Guan, M. (2023). Load deflection of flexible ring net barrier in resisting debris flows. *Géotechnique*, 1-13, e-First. https://doi.org/10.1680/jgeot.22.00135

Kong, Y., Zhao, J. D., & Li, X. Y. (2021). Hydrodynamic dead zone in multiphase geophysical flows impacting a rigid obstacle. *Powder Technology*, *386*, 335-349. https://doi.org/10.1016/j.powtec.2021.03.053

Marchi, L., Comiti, F., Crema, S., & Cavalli, M. (2019). Channel control works and sediment connectivity in the European Alps. *Science of the Total Environment*, *668*, 389–399. https://doi.org/10.1016/j.scitotenv.2019.02.416

Rossi, G., & Armanini, A. (2019). Impact force of a surge of water and sediments mixtures against slit check dams. *Science of The Total Environment*, *683*, 351-359. https://doi.org/10.1016/j.scitotenv.2019.05.124

Shan, T., & Zhao, J. (2014). A coupled CFD-DEM analysis of granular flow impacting on a water reservoir. *Acta Mechanica*, *225*(8), 2449–2470. https://doi.org/10.1007/s00707-014-1119-z

von Boetticher, A., Turowski, J. M., McArdell, B. W., Rickenmann, D., & Kirchner, J. W. (2016). DebrisInterMixing-2.3: a finite volume solver for three-dimensional debris-flow simulations with two calibration parameters–Part 1: Model description. *Geoscientific Model Development*, *9*(9), 2909-2923. https://doi.org/10.5194/gmd-9-2909-2016

Zhao, J., & Shan, T. (2013). Coupled CFD–DEM simulation of fluid-particle interaction in geomechanics. *Powder Technology*, *239*, 248–258. https://doi.org/10.1016/j.powtec.2013.02.003

Zhou, Z. Y., Kuang, S. B., Chu, K. W., & Yu, A. B. (2010). Discrete particle simulation of particle-fluid flow: Model formulations and their applicability. *Journal of Fluid Mechanics*, *661*, 482–510. https://doi.org/10.1017/S002211201000306X